ACS Catalysis

pubs.acs.org/acscatalysis Account

A Career in Catalysis: Xinhe Bao

Feng Jiao, Rentao Mu, Shutao Xu, Hongyang Liu, Liang Yu, Dunfeng Gao, Yuefeng Song, Dehui Deng, Guoxiong Wang, Heng Zheng, Weixin Huang, Xiulian Pan, Qiang Fu,* and Ding Ma*

Cite This: *ACS Catal.* 2025, 15, 3061−3084 Read Online

ACCESS | Metrics & More | Article Recommendations

Downloaded via DALIAN INST OF CHEMICAL PHYSICS on February 6, 2025 at 15:16:44 (UTC).
See https://pubs.acs.org/sharingguidelines for options on how to legitimately share published articles.

ABSTRACT: Professor Xinhe Bao has long been engaged in the research and development of heterogeneous catalysis and energy conversion processes. His research efforts have focused on discovering and elaborating the correlations between the structure, properties, and catalytic performance of nanocatalysts under nanoconfined conditions. Among his many achievements are the development of fundamental concepts for catalysis, establishment of in situ/operando characterization methods, and construction of high-performance catalyst systems. Specifically, he has proposed the concept of "nanoconfined catalysis", which has been successfully applied in spatially confined and interface-confined systems, and he has suggested the oxide−zeolite (OXZEO) process as an alternative technological platform for converting syngas to value-added chemicals and fuels. This account provides an overview of Professor Xinhe Bao's distinguished and ongoing career. We highlight several representative works from his team, although this report is not intended to be comprehensive.

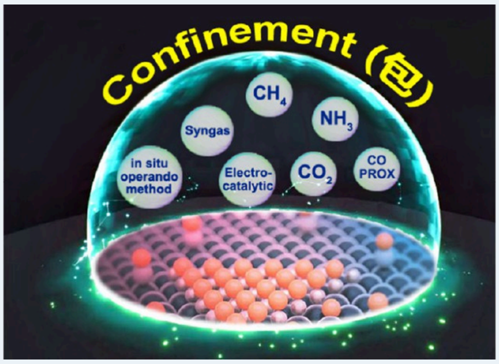

KEYWORDS: *Nanoconfined catalysis, C_1 chemistry, Electrocatalytic reactions, Surface science, In situ/operando characterization methods*

1. INTRODUCTION

Interestingly, in this instance, the subject area aligns with the name of the central figure. The three Chinese characters of 包信和 (Bao, Xinhe) nearly encapsulate both Professor Bao's academic contributions and his life (Figure 1).

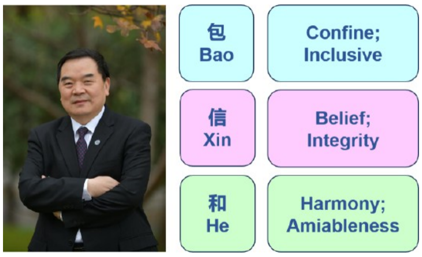

Figure 1. Photograph of Professor Xinhe Bao and the interpretation of his name in Chinese.

"包/**Bao**" in Chinese means "contain" or "confine". This coincides with Professor Bao's widely known catalytic concept of "Nanoconfined Catalysis". In addition, another meaning of "包" is "tolerant" and "inclusive". This is also the attitude of Professor Bao at work and the way he treats people, such as mentors, team leaders, directors of the institute, and presidents of the university. "信/**Xin**" on the one hand indicates "belief". His belief in science has encouraged Professor Bao to persevere in challenging research topics, such as C_1 chemistry, and make breakthroughs in the field. On the other hand, "信" also means "integrity". This principle serves as the foundation for Professor Bao's leadership of his team and the execution of academic research. "和/**He**" conveys the concepts of "harmony" and "amiableness". In addition, Professor Bao's harmonious relationship with his family has supported his intense research for decades. Further, the excellent relationship within his academic team has enabled efficient collaborative investigation and contributed to brilliant achievements in various fields. Almost everyone who encounters Professor Bao mentions his amiability.

Xinhe Bao was born in August 1959, in Yangzhong City, Jiangsu Province, China. In September 1978, he enrolled in the Department of Chemistry at Fudan University and pursued a doctoral degree after graduating with a bachelor's degree. Xinhe Bao received his PhD in Physical Chemistry from Fudan University in China in October 1987. Subsequently, he moved to Germany in 1989 and worked as an Alexander von Humboldt Research Fellow at the Fritz-Haber Institute, hosted by Professor Ertl. In May 1995, he returned to China and joined the Dalian Institute of Chemical Physics (DICP), Chinese

Received: November 3, 2024
Revised: January 25, 2025
Accepted: January 28, 2025

© XXXX American Chemical Society

https://doi.org/10.1021/acscatal.4c06765
ACS Catal. 2025, 15, 3061−3084

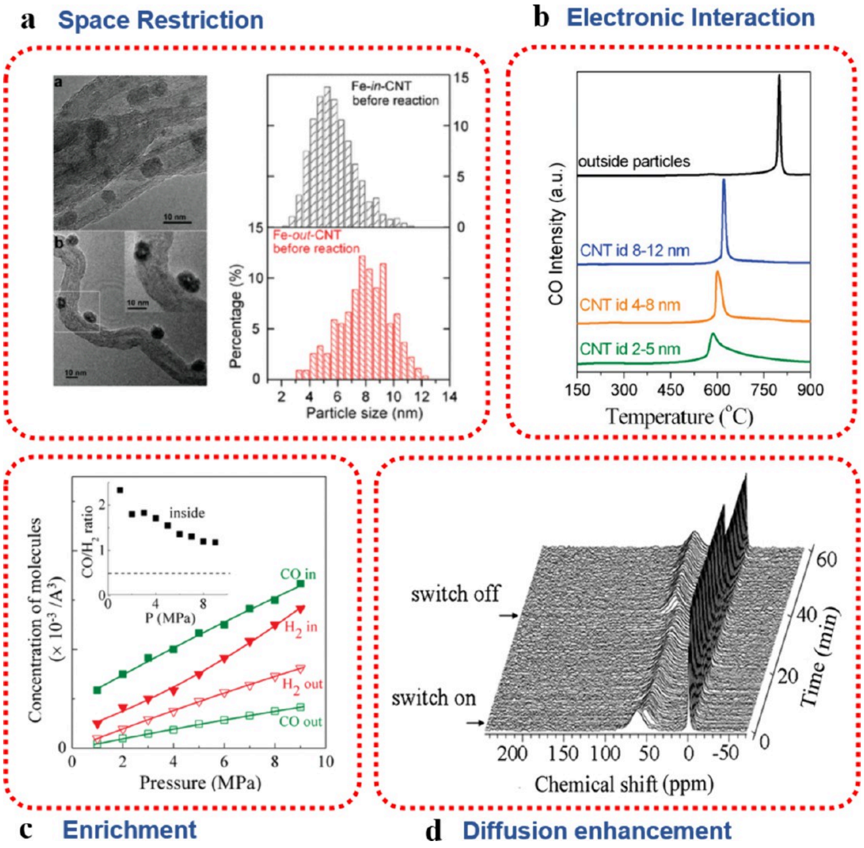

Figure 2. Confinement effect inside 1D channels of CNTs. (a) Transmission electron microscopy (TEM) images and particle size distribution of the activated catalysts with upper figures for Fe-*in*-CNT and lower figures for Fe-*out*-CNT before reaction. (b) Temperature-programmed desorption profiles under He atmosphere for the Fe_2O_3 particles confined inside the CNT channel with different inner diameters where Fe_2O_3 is reduced by carbon of CNTs.[2] (c) CO and H_2 molecule concentrations inside and outside of single-walled (SW)CNT(10, 10) as a function of pressure. The inset figure reveals the CO/H_2 ratio inside SWCNTs, with the dashed line representing the bulk ratio.[10] (d) NMR spectra show the ^{129}Xe signal at ∼66 ppm inside the SWCNTs during the adsorption and desorption of methanol at 0 °C. The 0 ppm signal corresponding to gas-phase ^{129}Xe.[5] Reproduced with permission from refs 2, 5, and 10. Copyright 2008, 2011, and 2009 American Chemical Society.

Academy of Sciences, where he established his research team and served as the director of the institute between 2000 and 2007. In March 2009, he was elected a member of the Chinese Academy of Sciences and appointed President of the Shenyang Branch of the Chinese Academy of Sciences. In July 2015, he was appointed Executive Vice President of Fudan University. In June 2017, he was appointed the President of the University of Science and Technology of China (USTC). He was also a deputy to the ninth, 10th, 12th, 13th, and 14th National People's Congresses and a member of the Standing Committee of the 13th and 14th National People's Congress.

Professor Xinhe Bao is primarily engaged in surface science and basic research on the catalytic chemistry related to energy-efficient conversion. He has published more than 700 peer-reviewed papers with more than 59,000 citations and has authorized over 200 patents. He has made remarkable achievements in several fields, including catalysis, surface science, C_1 chemistry, and electrocatalysis. Accordingly, he has won many honors. For instance, he was awarded the "Young Scientist" of Qiushi Foundation, Hong Kong, in 1996–2000, Ho Leung Ho Lee Foundation for scientific and Technological Progress Award in Chemistry in 2012, Outstanding Science and Technology Achievement Prize of the Chinese Academy of Sciences in 2015, Alwin Mittasch Prize of the German Catalysis Society in 2017, first national "Innovation Award" in 2017, Tan Kah Kee Science Award in Chemistry in 2018, First Prize of the National Natural Science Award in 2021, and National Catalysis Lifetime Achievement Award of China in 2023.

In addition to his outstanding success in scientific research, he has made important contributions to the field of catalysis by training young researchers. He has trained more than 150 PhD students, with more than 40 attaining professorships, and many of his students and postdoctoral researchers have emerged as significant figures in the global catalytic domain. In October 2024, Bao retired as the President of USTC. Shortly after his retirement, Professor Bao and his wife, Professor Guoyu Wang, made a public donation to the USTC to set up a "Foundation for Carbon Neutrality" in the university to support the development of young talent.

In the following sections, we provide an overview of his distinguished contribution to the field of catalysis and highlight some milestones from his team.

2. NANOCONFINED CATALYSIS

One of Bao's most widely known contributions to the science of catalysis is the proposal and development of the concept of nanoconfined catalysis.[1−7] "Confinement" denotes the condition of being restricted to a specific area, the action of being restricted, or a state of restriction.. Owing to the restriction of a certain physical state, the intrinsic structure and electronic characteristics of a catalytic system change, thereby altering the catalytic performance. Professor Bao's team has made

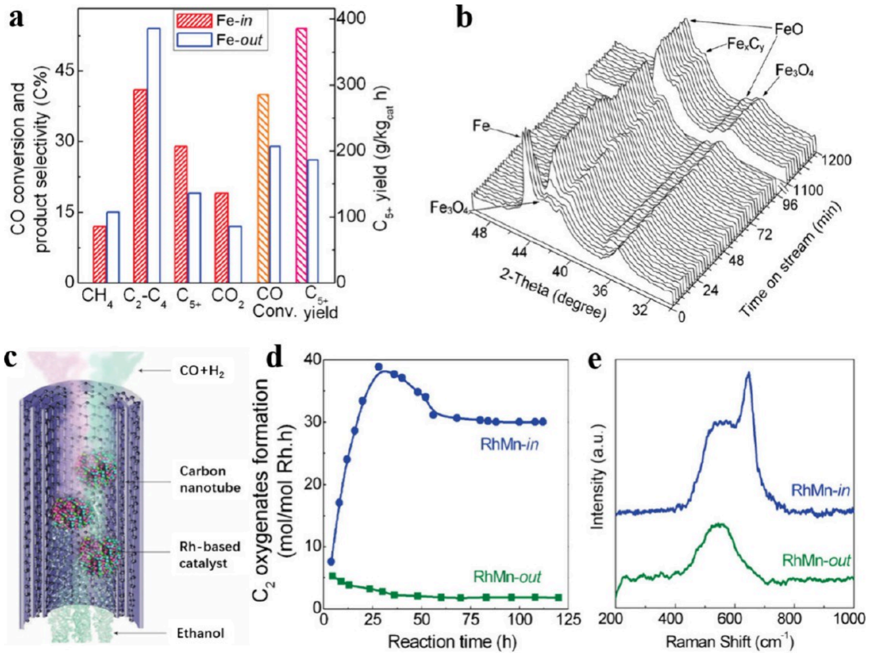

Figure 3. (a) Confinement effect of CNTs on the iron based FTS activity and (b) crystal-phase evolution of Fe-in-CNTs in syngas.[2] Reproduced with permission from ref 2. Copyright 2008 American Chemical Society. (c) Scheme of syngas conversion to C_2 oxygenates using encapsulated RhMn nanoparticles inside CNT channels. (d) Comparison of C_2 oxygenates formation rate from syngas over RhMn catalysts. (e) Raman spectra of RhMn catalysts upon CO adsorption.[1] Reproduced with permission from ref 1. Copyright 2007 Springer Nature.

continuous efforts in this field for almost 30 years. This nanoconfined concept almost runs through his research in various fields of catalysis. In 2020, Professor Bao won the highest science and technology award in China, which was the first prize in National Natural Science, based on his nanoconfinement concept.

2.1. Confined Catalysis in One-Dimensional Nano-channels.

According to the literal meaning of the word "confinement", one may first think about the active catalyst component being in a restricted space. A representative example is the catalytic effect confined within a one-dimensional (1D) channel of carbon nanotubes (CNTs). CNTs, which are rolled-up graphene layers, are well-known for their unique tubular morphology and well-defined structure.[3,5] Due to the curvature, the π electron density in the graphene layers moves from the concave inner surface to the convex outer surface, creating an electrical potential difference across the walls of the carbon nanotube (CNT). Professor Bao anticipated that the confined rigid channel of CNTs could provide intriguing possibilities for introducing other active species, which may lead to nano-composite materials having catalytic behavior different from those on the outside or in the bulk phase, thus providing new opportunities for heterogeneous catalysis.

In general, the confinement effect within CNTs can be refined in four ways. The first is the restriction of the geometric space of the CNT channel inside the metal nanoparticles, which hinders their migration and aggregation during the catalytic reaction process.[8] Therefore, the confined metal particles maintain their small size during the reaction (Figure 2a).[2] Second, the electronic properties of the nanoparticles confined inside the channel, such as the oxidation−reduction properties, change owing to the electron-deficient environment. For example, the reduction temperature of Fe_2O_3 nanoparticles assembled in <12 nm CNT channels is approximately 200 °C lower than that of outside Fe_2O_3 nanoparticles. In addition, the reduction temperature of the inside Fe_2O_3 decreases as the CNTs inner diameter decreases from 8−12 to 2−5 nm (Figure 2b). DFT calculations shown that the d-band states of the metal clusters encapsulated inside CNTs are downshifted compared to those residing on the exterior walls. This downshift, caused by electronic effects, results in weakened binding energies between oxygen and the encapsulated metal clusters. Such oxygen is more likely to be removed by reductant, and thus the confined oxide is more easily reduced.[9] Third, the confined space of the CNTs results in a unique enrichment in the local concentration of small molecules. For example, the theoretical simulation results show that CO and H_2 can be gathered inside the tubes, and the apparent pressure difference between the inside and outside of the tube is three to five times when a (10,10) double-walled tube is considered (Figure 2c).[10] In addition, the diffusion characteristics of some product molecules also change significantly inside the CNT channels. CNT was first exposed to pure ^{129}Xe. Thereby it was switched to a mixture of ^{129}Xe and methanol (switch-on mark in Figure 2d). Methanol gradually displaced ^{129}Xe and occupied the CNT channels. As a result, the intensity of inside ^{129}Xe signal declined (~66 ppm). After methanol was switched off, the ^{129}Xe intensity increased accompanied by methanol desorption (Figure 2d). Accordingly, the diffusion rate of methanol molecules in the CNTs is five times that outside the tube and 8−50 times that of Si−Al mesoporous materials with similar diameters (Figure 2d). A high diffusion rate within CNTs is likely attributed to reduced friction and weakened hydrogen bonds among the methanol molecules.[5]

Combined with the above effects, CNT-confined metal nanoparticle catalysts exhibit unique catalytic properties that have applications in numerous fields, such as syngas conversion,[1,2,11−13] ammonia synthesis and decomposition,[9,14,15] selective oxidation, and electrocatalysis.[16−19] One representative example is the promotion of Fischer−Tropsch synthesis (FTS) catalysis using CNT-confined iron catalysts

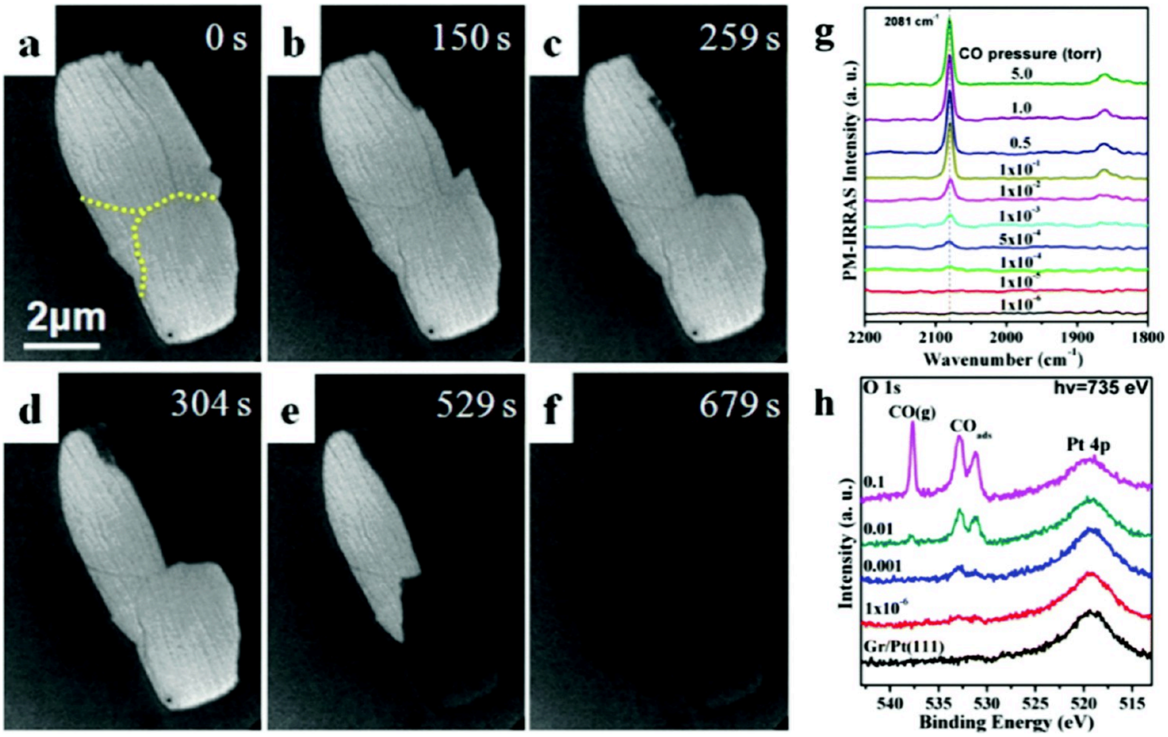

Figure 4. CO intercalation between graphene flakes and a full graphene layer on Pt(111) at room temperature. (a−f) Series of low-energy electron microscopy (LEEM) images recorded from a Pt(111) support single-layer graphene island after exposed to 1×10^6 mbar CO at room temperature at the indicated exposure times. Wrinkles are marked with yellow dashed lines in (a).[20] Reproduced with permission from ref 20. Copyright 2012 John Wiley and Sons. (g) In situ polarization-modulated infrared reflection−absorption spectroscopy (PM-IRRAS) study on CO adsorption on 1 monolayer (ML) Gr/Pt(111) surface. (h) In situ near-ambient pressure X-ray photoelectron spectroscopy (NAP-XPS) O 1s spectra from the 1 ML Gr/Pt(111) surface exposed to UHV, 1×10^6, 0.001, 0.01, and 0.1 Torr CO, respectively.[21] Reproduced with permission from ref 21. Copyright 2014 National Academy of Sciences.

(Figure 3a).[2] The metallic iron species encapsulated inside the CNTs preferentially transform into iron carbides under the reaction conditions, which is essential for obtaining high FTS activity (Figure 3b). Notably, the C_{5+} hydrocarbons yield over the confined iron catalyst was double that over the iron catalyst outside the CNTs and more than six times higher than that of the iron catalyst supported on activated carbon.

Thereafter, Bao et al. further extended this strategy for syngas conversion to ethanol by encapsulating RhMn nanoparticles inside the CNT channels (denoted as RhMn-in), resulting in a striking enhancement in the catalytic activity (Figure 3c).[1] The overall formation rate of ethanol reached 30.0 $\text{mol/mol}^{-1}_{\text{Rh}}\ \text{h}^{-1}$ inside the CNTs, exceeding the RhMn supported on the outside of CNTs by more than 10 times, although the latter was much more accessible to the reactants (Figure 3d).

In addition, the Raman spectra (Figure 3e) indicate that the activated CO may have been modified inside the CNTs. Specifically, new Raman bands corresponding to the Mn−O (~640 cm^{-1}) bonds were observed for only RhMn-in when both catalysts were exposed to CO. Because oxophilic Mn may remain in a more reduced state within the CNT channels, it could facilitate CO dissociation and, thus, achieve a significantly higher C_2 oxygenate formation rate with respect to the outside Mn species.

2.2. Confined Catalysis in Two-Dimensional Nanospaces.

The space between two-dimensional (2D) overlayers and solid surfaces can serve as a special confined environment for catalytic reactions. First, the distance between the 2D overlayer and the substrate typically ranges within nanometers. Atoms or molecules within this narrow space experience significant confinement, especially in the direction perpendicular to the substrate surface. Moreover, all intercalated atoms or molecules simultaneously interact with both the upper and lower boundaries, which are influenced by the weak interactions between the 2D layer and the substrate. Consequently, the surface chemistry of molecules and their reactions on solid surfaces are profoundly impacted by the presence of the 2D overlayer, demonstrating a pronounced 2D-confinement effect that distinguishes these reactions from those occurring on open surfaces.

Professor Bao's team first observed the CO intercalation of monolayer graphene islands grown on a Pt(111) surface at room temperature with a CO pressure (pCO) in the range of 10^{-6} mbar. The intercalated CO can desorb from the Pt surface at around room temperature under ultrahigh vacuum (UHV) (Figures 4a−f). In contrast, CO remains on the open Pt surface up to 423 K. This finding indicates that the graphene layer exhibits a strong confinement effect on the chemistry of the molecules below.[20] Later, they observed that surface reactions such as CO oxidation can occur on a Pt(111) surface covered by monolayer graphene sheets. Combining the surface science measurements and density functional theory (DFT) calculations, they demonstrated that the strong interaction between CO and Pt can be weakened by the graphene overlayer. Consequently, it facilitates CO oxidation with a lower apparent activation energy (Figures 4g and 4h). These results indicate that the interfaces between the graphitic overlayers and metal surfaces act as 2D-confined nanoreactors, in which catalytic reactions are promoted.[21]

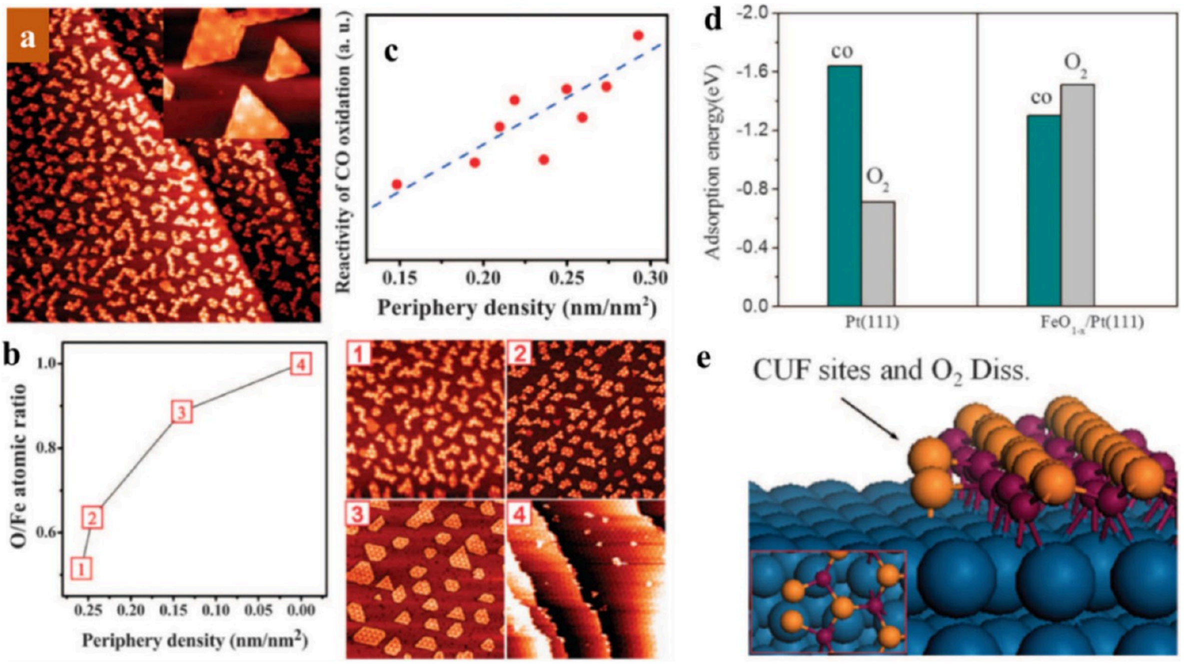

Figure 5. (a) STM image (200 nm × 200 nm) of FeO_{1-x} nanoislands on Pt(111). (b) O/Fe atomic ratio with different peripheral densities of FeO_{1-x} nanoislands. (c) CO oxidation reactivity as a function of the peripheral density of FeO_{1-x} nanoislands. (d) Calculated adsorption energy for CO and O_2 molecules. (e) Calculated transition state of O_2 dissociation at FeO–Pt(111) boundary.[4] Reproduced with permission from ref 4. Copyright 2010 American Association for the Advancement of Science.

Bao et al. demonstrated by using DFT calculations that the adsorption of atoms and molecules on a Pt(111) surface is consistently weakened when covered by a monolayer of graphene. This effect can be attributed to geometric constraints and confinement within the 2D space between the graphene overlayer and the Pt(111) surface. Similar results were observed for Pt(110) and Pt(100) surfaces coated with graphene. Notably, the microenvironment created by covering a catalyst surface with a 2D material can modulate surface reactivity, as exemplified by optimizing the oxygen reduction reaction activity on Pt(111) coated with various 2D materials. Accordingly, the confined catalysis concept under a 2D cover has been suggested, which is based on weak van der Waals interactions between 2D material overlayers and the underlying catalyst surfaces. The 2D nanospaces under graphene provide an intriguing confinement environment for surface chemistry and catalysis.[22]

Overall, Professor Bao's research regarding the confinement effects of 2D cover has led to new chemistry in small spaces, such as "catalysis under cover" and "electrochemistry under cover". These new concepts enable the design of advanced nanocatalysts encapsulated in 2D material shells, which may improve the performance of many important heterogeneous catalysis, electrochemistry, and energy conversion processes.[23]

2.3. Confined Catalysis at Interfaces. Coordinatively unsaturated (CUS) metal sites are often considered catalytically active centers in enzymes and homogeneous catalysis. Typically, CUS active sites consist of transition metal cations in intermediate valence states. This structural characteristic facilitates moderately strong bonding between reactive species and the active sites, aligning with the Sabatier principle. For instance, metallic Fe atoms exhibit significantly higher activity in O_2 dissociation compared to Pt atoms. However, in several reactions involving molecular oxygen, metallic Fe atoms do not show superior catalytic performance compared to Pt atoms. This occurs because the strong interaction between metallic Fe atoms and oxygen results in the formation of stable iron oxides, such as Fe_2O_3. Consequently, the metals lose their CUS characteristics and catalytic activity. Therefore, a key challenge in catalysis is maintaining the CUS state of transition metal cations throughout the catalytic reactions. The intrinsic interaction between the active sites and their local environment prevents the degradation of the CUS state, an effect known as confinement. This can be enhanced by specific crystal structures and the electronic properties of nanoscale environments.

Inspired by this, Bao et al. described a strategy for interface confinement to stabilize nanostructured ferrous oxides (FeO) on the surface of a Pt substrate.[4] Scanning tunneling microscopy (STM) studies showed that the interface-confined FeO nanoislands were monolayer-dispersed on a Pt(111) substrate (Figure 5). As shown in Figure 5b, the O/Fe atomic ratio increased as the peripheral density of the FeO nanoislands decreased, indicating that there were several coordinatively unsaturated ferrous (CUF) sites at the edges of the 2D FeO nanoislands. To test the reactivity of the model surfaces, samples presaturated with CO were monitored using ultraviolet photoelectron spectroscopy (UPS) in an O_2 atmosphere at room temperature. The reactivity for CO oxidation was plotted as a function of the peripheral density of the FeO nanoislands, and a linear relationship between the catalytic reactivity and the peripheral density of the FeO nanoislands was observed (Figure 5c). This finding clearly indicates that the CUF sites at the edges of the FeO nanoislands are the active sites for CO oxidation. DFT calculations provided further insight into the origin of the high reactivity of the FeO_{1-x}/Pt(111) surface. As shown in Figure 5d, the adsorption energies of CO and O_2 on Pt(111) are −1.64 and −0.71 eV, respectively. This is consistent with the experimental observation of CO poisoning in Pt(111) at modest temperatures. However, on the CUF sites, the adsorption energy of O_2 is increased to −1.51 eV, higher than the adsorption energy of CO. Therefore, the superior catalytic performance of the $FeO_{1-x}/Pt(111)$ surface can be attributed to the preferential adsorption and facile activation of O_2 at the CUF sites at the edges of the FeO_{1-x} nanoislands (Figure 5e). The calculation results also show that the dissociative adsorption of H_2 on CO-precovered Pt(111) and FeO is difficult at room temperature, indicating that this FeO_{1-x}/Pt catalyst can efficiently catalyze the preferential oxidation of CO in excess H_2 (PROX).[4]

The above-mentioned interface confinement can stabilize the metastable FeO_{1-x} structure and CUS Fe active sites at the edges of the oxide nanoislands over a wide range of temperatures and O_2 pressures. To describe the interface interaction between the oxide and metal quantitatively, the interface confinement energy ($E_{\mathrm{confinement}}$) was defined (Figure 6), which originates from the orbital hybridization between Pt and Fe. Furthermore, the concept of the interface confinement effect has been widely applied to numerous other oxide−metal catalytic systems and can guide the rational design of novel active centers. For the oxide layer, monolayer-dispersed CoO, NiO, MnO, ZnO, and CeO_2 nanoislands were prepared on metal substrates. Metal substrates can be extended to Au, Ru, Pd, Ag, Cu, and carbides.[6,24]

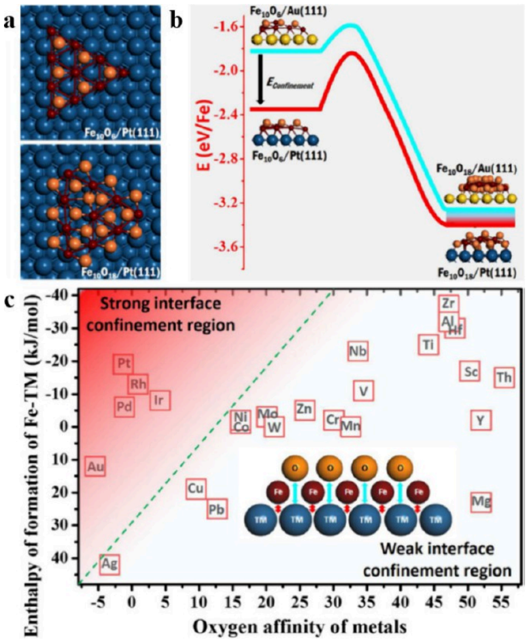

Figure 6. (a, b) DFT calculations of FeO oxidation on Au(111) and Pt(111) surfaces. (c) Interface confinement effect in FeO_x/transition metal inverse systems. The dashed line reflects the borderline between the strong and weak interface confinement effects.[24] Reproduced with permission from ref 24. Copyright 2015 American Chemical Society.

Currently, the most frequently used catalysts for CO PROX reactions are Pt and transition metal oxides. To reduce the use of Pt, Bao et al. prepared a sandwich-structured catalyst with an FeO-on-Pt shell deposited on a Cu core (FeO-on-Cu@Pt). In the FeO-on-Cu@Pt structure, the amount of loaded Pt could be decreased from 4 to <1 wt %, but the catalytic performance remained similar to that of the original FeO-Pt catalyst. In situ X-ray adsorption spectroscopy (XAS) studies of this catalyst during the CO PROX reaction at room temperature revealed the presence of CUS Fe species on Pt, indicating that the interfacial confinement effect on bulk Pt is also effective on ultrathin Pt shells. The secondary components under the Pt shell not only reduce the usage of Pt but also improve the CO PROX performance by weakening CO adsorption on the Pt surface.[25,26] In addition, DFT calculations predicted that the OH groups or alkali metal species on the oxide surface may affect the interfacial interactions between the ultrathin oxide nanoislands and the metal substrate. Recently, STM and XPS measurements have shown that the hydroxyl groups on the surface of the CoO nanoislands can make the CoO nanoislands more resistant to further oxidation in O_2 by enhancing the interface confinement effect on the CoO/Pt(111) system.[27]

2.4. From Spatial Confinement to General Confinement. As discussed above, confinement is an important concept for modulating the chemical properties of catalysts and energetic processes. Crucially, the fundamental physical and chemical properties of atoms, molecules, and clusters can undergo significant changes when confined in small spaces, such as 0D zeolites, 1D carbon nanotubes, and 2D interlayers (Figure 7).

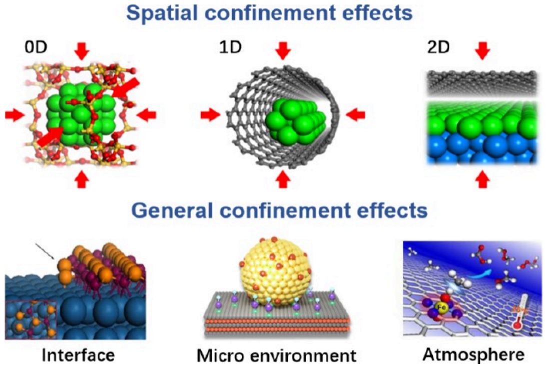

Figure 7. Schematic of the nanoconfined catalysis concept. From spatial confinement to general confinement effects, i.e., the effect of the interface, microenvironment, and atmosphere.[4,28,29] Adapted with permission from ref 4. Copyright 2010 American Association for the Advancement of Science. Adapted with permission from ref 28. Copyright 2013 John Wiley and Sons. Reproduced with permission from ref 29. Copyright 2018 Elsevier.

This confinement often results in novel chemical behavior and enhanced performance. The confinement effect can be intuitively understood as a spatial phenomenon where the nanocavity imposes geometric constraints on the guest molecules. Additionally, electronic interactions or interfacial bonding between the nanocavity walls and the guest can modulate its atomic and electronic structures, leading to the formation of metastable structures like CUSs, which exhibit enhanced reactivity. A similar interaction also takes place between a guest atom, molecule, or cluster and an open host surface. Confinement by an open surface or interface has also been observed. Studies have shown that metastable guest nanolayers, containing CUSs, can be stabilized on an open host surface. This is exemplified by the formation of defective oxide nanoislands on noble metal surfaces. Therefore, an open solid surface can exert a similar confinement effect to stabilize CUSs, akin to that of enclosed nanospaces. Consequently, the concept of confined catalysis can be broadened from merely spatial confinement to a more general confinement effect (Figure 7), where the interface, microenvironment, and even the reaction atmosphere play crucial roles.

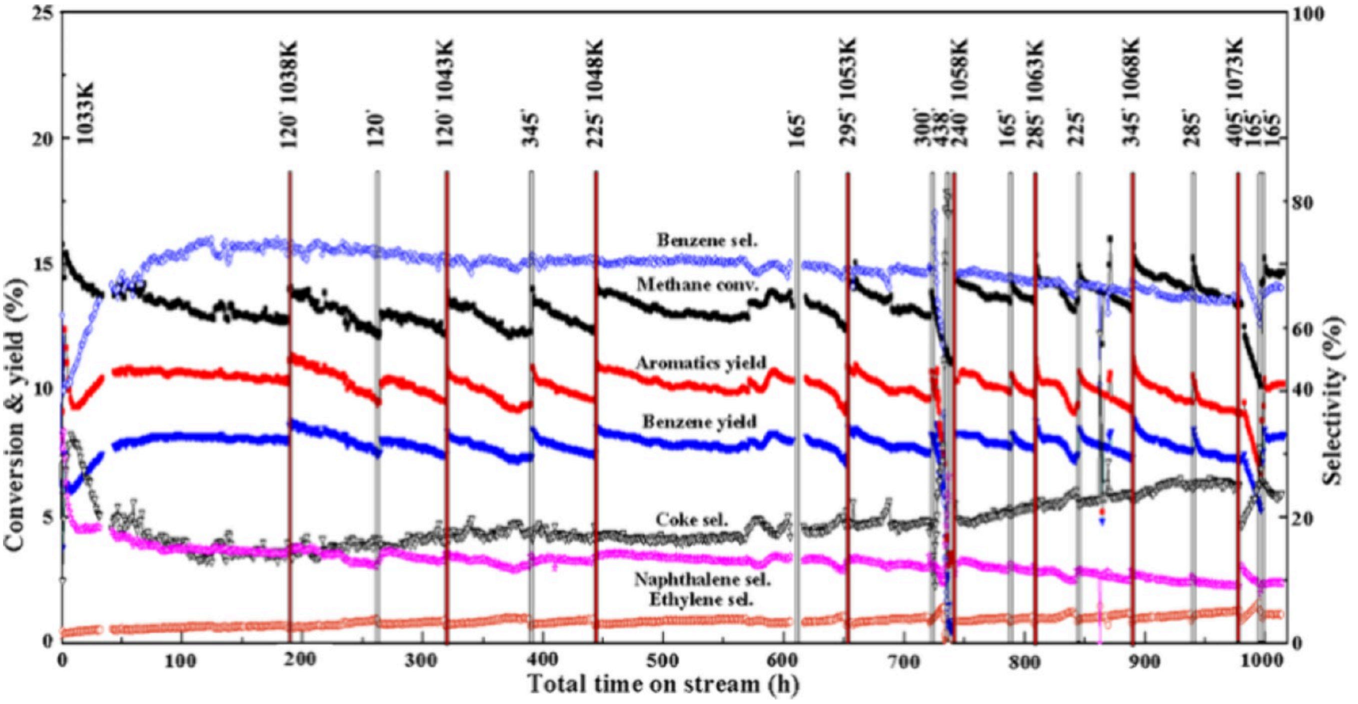

Figure 8. Long-term stability test of Mo/ZSM-5 for MDA reaction between 1033 to 1073 K, with a periodic switch between CH_4/N_2 and H_2.[41] Reproduced with permission from ref 41. Copyright 2015 Elsevier.

3. HETEROGENEOUS THERMAL CATALYSIS IN C_1 CHEMISTRY

Professor Bao has dedicated himself to the field of C_1 chemistry. His studies have provided a fundamental understanding of selective catalytic oxidation reactions, as well as application-oriented methane conversion and CO hydrogenation to valuable chemicals and fuels. Here, we summarize a few examples.

3.1. Methane Conversion. When Bao finished his postdoctoral work in Germany and returned to the DICP, China, in 1995, Wang et al. at the DICP had just developed a new nonoxidative methane dehydroaromatization (MDA) process.[30] Compared to traditional selective methane oxidation, the new process enabled the conversion of methane into aromatics and hydrogen with much higher benzene selectivity under oxygen-free conditions using a Mo/ZSM-5 catalyst. More importantly, the process resolved a key challenge: the excessive oxidation of methane. Therefore, Professor Bao chose nonoxidative methane conversion as one of his major research projects and has studied this area for nearly 30 years.

Over the years, extensive research has led to significant progress in this field. However, the greatest challenge facing this process is its poor stability owing to severe coke deposition, which can cover the active sites and even block the pores and channels of the zeolites.[31,32] Therefore, Professor Bao's team has also made many efforts to search for approaches to extend the lifetime of catalysts and explore regeneration methods. For example, they designed a Mo/MCM-22 catalyst for MDA, which exhibited similar activity but higher benzene selectivity than the widely used Mo/HZSM-5 catalyst under the same reaction conditions.[33−40] Notably, the unique pore architecture of MCM-22, which has large 3D 12-membered ring (MR) supercages interconnected by 10MR windows, inhibited the formation of undesired naphthalene and coke to a greater extent than ZSM-5. In addition, they demonstrated that hydrogen treatment is an effective regeneration method for the hydrogenation of coke, thus extending catalyst lifetime. As shown in Figure 8, a 1000-h stability test of MDA with a periodic switch of CH_4/N_2 to H_2 was conducted using a nanosized HZSM-5-supported Mo catalyst at 1033−1073 K.[41]

However, coke hydrogenation cannot completely eliminate its deposition; that is, coking cannot be completely suppressed, even with periodic oxygen combustion. Therefore, Bao has continuously explored more effective catalysts and reaction pathways to convert methane under nonoxidative conditions without coke deposition. Serendipitously, Bao and colleagues found a catalyst showing excellent resistance to carbon accumulation during high-temperature methane conversion.[42] Professor Bao was acutely aware that this phenomenon might be highly important in the field. Therefore, he led the team to conduct extensive studies to optimize the catalyst and elucidate its catalytic mechanism. The results revealed that single iron sites confined in a nonacidic silica matrix, with an iron atom bonded to two carbon atoms and one silicon atom, play a decisive role in the direct nonoxidative conversion of methane to olefins, aromatics, and hydrogen (Figure 9a, denoted MTOAH).[42] This reaction is initiated by the catalytic C−H dissociation of methane over single Fe sites, forming methyl and surface H species. Because there are no adjacent iron sites, these methyl species cannot pass through the surface C−C coupling route. As a result, surface oligomerization and coke deposition are effectively inhibited. Alternatively, the surface methyl species desorb as methyl radicals in the gas phase, where they couple to form ethane. Thus, ethane is readily dehydrogenated to ethylene without a catalyst (Figure 9b). At 1363 K, the methane conversion reached a maximum of 48.1%, and the ethylene selectivity peaked at 48.4%, whereas the total hydrocarbon selectivity exceeded 99%. This represents an atom-economic methane transformation process (Figure 9c). Crucially, the lattice-confined single iron sites exhibited stable performance throughout the 60-h test, with no signs of deactivation. Since its

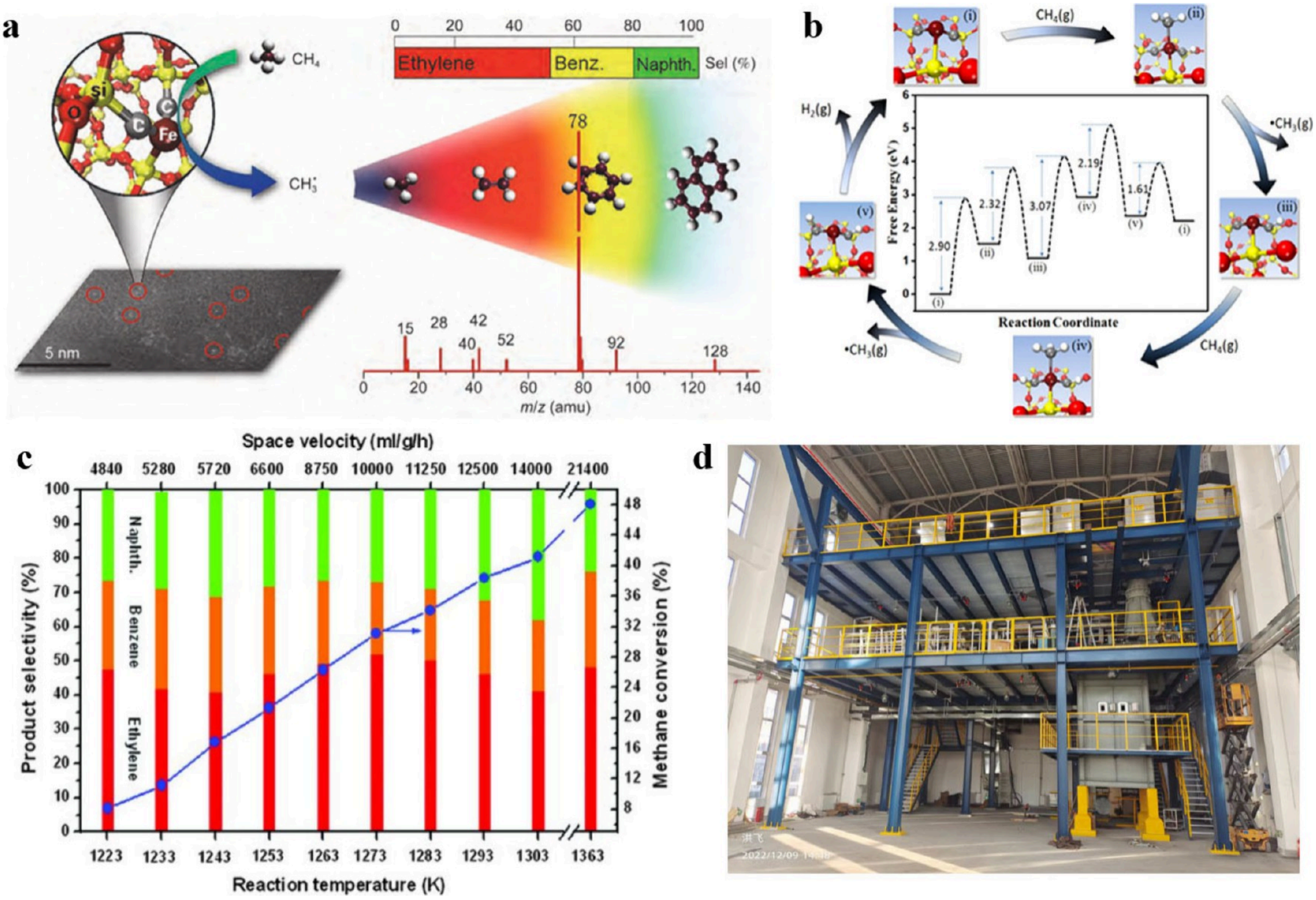

Figure 9. (a) Schematic of the MTOAH reaction using single iron sites embedded in a silica matrix. (b) Reaction mechanism of methane conversion over Fe©SiO_2 at 1223 K based on DFT calculations. (c) Reaction performance of Fe©SiO_2 catalyst in the MTOAH reaction. Reaction temperature from 1223 to 1363 K and space velocity from 4840 to 21400 mL/g h.[42] (d) Photo of MTOAH pilot plant with 500 t of methane processing capacity per year at the Changxing Island campus of DICP. Reproduced with permission from ref 42. Copyright 2014 American Association for the Advancement of Science.

first report, MTOAH has attracted worldwide attention.[32,43−51] Invited by BASF in 2015, Professor Bao led the team to demonstrate the catalytic performance of MTOAH using their benchmark catalyst at BASF's headquarters in Ludwigshafen.

In addition to fundamental studies to understand the mechanism of this catalytic process, the industrial scale-up of this new technology has been studied by Professor Bao and his team. In 2016, a tripartite R&D team including China National Petroleum Corporation (CNPC), Saudi Basic Industry Corporation (SABIC), and Professor Bao was formed. They established a scale-up laboratory on the Changxing Island campus of the DICP and developed four generations of catalysts and reactors for industrial scale-up. In 2018, they completed a laboratory-based 1000-h single-tube stability evaluation, with no deactivation observed. With the financial support from the "13th Five-Year Plan" Science and Education Infrastructure Construction Project of the Chinese Academy of Sciences, they further built a MTOAH pilot plant with 500 t of methane processing capacity per year at the Changxing Island campus of the DICP (Figure 9d). The equipment is currently undergoing joint debugging and is expected to be operational by the end of the year.

In addition to nonoxidative methane conversion under high reaction temperatures, Bao et al. also explored novel reaction routes for the selective oxidation of methane under mild conditions. For instance, they have developed a novel catalytic system that integrates three redox couples—Pd^{2+}/Pd^0, quinone/hydroquinone, and NO_2/NO—in CF_3COOH. This system, for the first time, incorporates an organic cocatalyst to achieve the selective oxidation of methane at 80 °C, significantly enhancing the catalytic efficiency of transition metals.[52]

In addition, Bao et al. developed graphene-confined FeN_4 sites that exhibited high activity for the conversion of C−H bonds under mild conditions, such as the oxidation of CH_4 or C_6H_6 by H_2O_2 to C_1 oxygenates or phenol, respectively.[29] They showed that the generated active oxygen species on the FeN_4 sites could directly activate and dissociate the C−H bonds of CH_4 or C_6H_6 at room temperature. Notably, the graphene-confined FeN_4 site was first observed using STM characterization, confirming the presence of active sites.

3.2. Syngas Conversion. Professor Bao is renowned for his impactful work in syngas conversion, a process utilizing syngas, a CO and H_2 mixture, as a vital feedstock for catalytically harnessing diverse carbon resources. For example, he has been involved in direct syngas conversion since the 2000s, and his involvement continues to this day.

Based on years of study and understanding in the field of syngas conversion via FTS, Professor Bao clearly recognized that the drawbacks of FTS arise from its reaction mechanism. Both the CO and H_2 activation steps, as well as the C−C coupling of

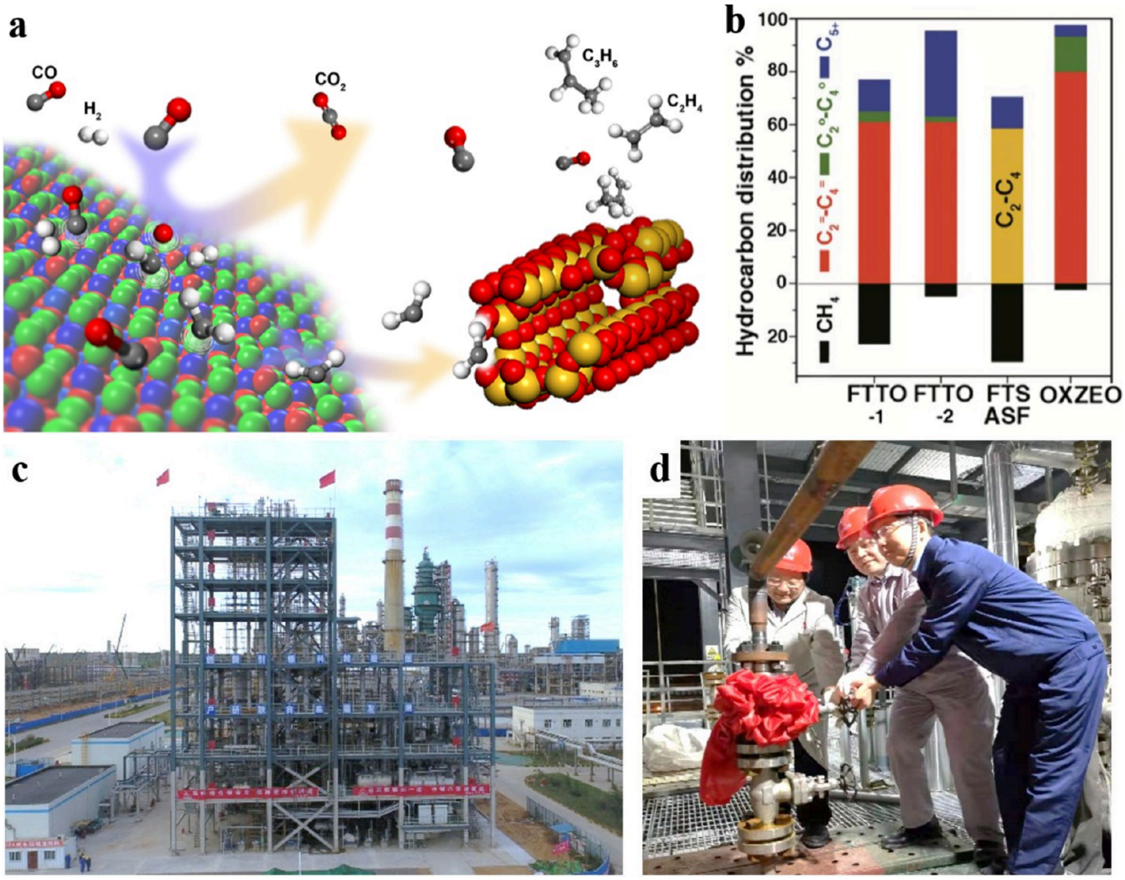

Figure 10. Syngas conversion to light olefins within the OXZEO bifunctional catalyst concept. (a) Schematic and (b) hydrocarbon distribution in comparison to the ASF distribution in conventional FTS and representative Fe-based FTTO-1 catalysts and Co-based FTTO-2 catalyst.[54] Adapted with permission from ref 54. Copyright 2016 American Association for the Advancement of Science. (c) Photo of the first OXZEO-TO pilot plant with an output of 1000 t of light olefins per year in Shannxi, China. (d) Photo of Professor Bao opening the feed gas valve during the pilot test.

the surface CH_x building blocks, occur over the same metal or metal carbide open surface of the FTS catalyst. Consequently, the carbon chain length distribution of the products follows a statistical mathematical model, namely the Anderson−Schulz−Flory (ASF) model.[53] For example, the selectivity for C_2 to C_4 hydrocarbons, including olefins and paraffins, did not exceed 58%. Professor Bao was an early advocate of thinking creatively about the classical FTS process and exploring new reaction pathways to achieve high selectivity beyond the ASF limit.

For example, Bao et al. designed a bifunctional catalyst based on a metal oxide and zeolite, namely the oxide−zeolite (OXZEO) catalyst, instead of using metals or metal carbides as the FTS catalyst.[54−73] In the OXZEO catalytic process, the activation of CO and H_2, as well as the generation of active intermediates, was conducted over a partially reduced metal oxide surface. Subsequently, the intermediates desorbed into the gas phase and diffused into the confined channels of the zeolites (or zeotypes), where C−C coupling occurred to form hydrocarbon products. Thus, direct syngas conversion is spatially separated into a tandem process with two active centers that respond to feedstock activation and hydrocarbon product formation (Figure 10a).[54] For example, a bifunctional composite with a partially reduced $ZnCrO_x$ oxide and mesoporous SAPO-34 zeotype enabled direct syngas conversion to light olefins with selectivity as high as 80% at a CO conversion rate of 17%. The C_2−C_4 hydrocarbons, including olefins and paraffins, increased beyond 90%. This result significantly exceeds both the ASF model's prediction of 58% and the yields obtained in the FTS-to-light-olefins (FTTO) process, which are 61% over either Fe- or Co-based catalysts (Figure 10b). The excellent product selectivity of OXZEO, beyond traditional FTS, has also attracted attention from industry. Shortly after the publication of the OXZEO concept in 2016, Bao's team cooperated with the applied development team led by Zhongmin Liu at the DICP and developed industrially scaled-up catalysts and technology for direct syngas conversion to light olefins (OXZEO-TO). They further cooperated with the Yanchang Petroleum Group to demonstrate the first industrial pilot test with an annual output of 1000 t of light olefins in 2020, which further verified the scientific principle and feasibility of the process (Figures 10c and 10d).[72]

To gain insight into the mechanism of the novel OXZEO process. Professor Bao's team conducted systematic studies on the metal oxide and zeolite components. Using in situ ambient-pressure XPS and temperature-programmed experiments, it was found that $ZnCrO_x$ could be partially reduced in H_2 and CO.[54] Thus, CO was activated and dissociated, producing surface carbon species and CO_2 as products. The surface carbon species can be further hydrogenated with surface hydrogen to produce a clean surface for further catalytic cycles. Highly sensitive synchrotron-based vacuum ultraviolet photoionization mass spectrometry (SVUV-PIMS) measurements confirmed the presence of gas phase intermediate ketene (CH_2CO) in the syngas conversion reactor effluent using $ZnCrO_x$ as catalyst, evidenced by a mass-to-charge (m/z) signal at 42.01 at a photoionization energy of $h\nu = 9.72$ eV. Thereafter, these active intermediates can be transported through the gas phase to the confined zeolite channel and further converted into light olefins.

Because ketene conversion is controlled by zeolites, their topology and acidity can be modulated to turn the OXZEO concept into a general strategy for direct syngas conversion to produce a range of value-added chemicals and fuels (Figure 11). For example, SAPO-34,[54,55,58,64,65] SAPO-18,[62,73] and SAPO-17,[71] which have 8-MR pores, allow the selective synthesis of mixed light olefins. The 8-MR side pocket of mordenite zeolite (MOR), which is smaller than the CHA-cage, favored ethylene formation.[57] In comparison, zeolites/zeotypes having 10-MR and 12-MR pores, such as ZSM-5, SAPO-11, ZSM-11, ZSM-22, and ZSM-12, favor the formation of gasoline-range hydrocarbons (C_5-C_{11}).[59,68,69,74,75]

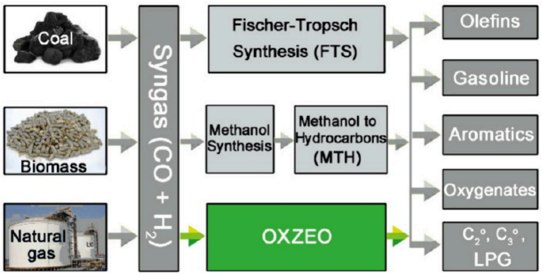

Figure 11. Scheme for syngas conversion to value-added chemicals and fuels.[72] Reproduced with permission from ref 72. Copyright 2021 American Chemical Society.

Thus, OXZEO has become an alternative platform for the better utilization of carbon resources via syngas. This has inspired the further development of highly efficient bifunctional catalysts for syngas conversion and CO_2 and hydrocarbon utilization.[72]

Although considerable success has been achieved using the OXZEO strategy in tackling product selectivity, CO conversion and the space−time yield of current OXZEO catalysts require improvement. Therefore, efforts have been made to optimize these catalysts by screening a wide range of metal oxide/zeolite (or zeotype) combinations and reaction conditions. With these efforts, the activity has improved. For example, CO conversion has been increased from 17% to 60% while the light-olefin selectivity was maintained at 75%, and the yield of light olefins has been increased from 8% to 27%. However, further improvement of OXZEO has stalled because of the activity−selectivity trade-off (red dashed line in Figure 12a), having a maximum yield of 27% light olefins, including either OXZEO or FTTO catalysts.[66]

This collection of long-term studies led Professor Bao to realize that the catalytically active Si−OH−Al bridge hydroxyl acid sites in zeolites (or zeotypes) of the OXZEO catalyst not only catalyze the target reaction of the C−C coupling of ketene intermediates to olefins but also catalyze the side reactions of olefins to undesired products via excessive hydrogenation and oligomerization. This common active center acts like the fulcrum of a "seesaw" (Figure 12b).[66] That is, when the conversion rate increases, the selectivity decreases. Therefore, simultaneous improvement of conversion and selectivity cannot be achieved, resulting in a low light-olefin yield. To terminate the reaction at the olefin formation step, it is necessary to develop a novel catalyst system and separate the target C−C coupling of ketenes from the secondary reactions of hydrogenation and oligomerization of olefins.

After several years of perseverance, the team discovered that substituting Ge into AlPO-18 is an effective strategy to achieve this goal, thereby breaking the activity-selectivity trade-off. Crucially, the attenuated Ge−OH−Al Brønsted acid sites are largely inactive for secondary reactions, such as the hydrogenation and oligomerization of olefins, and increasing the density of Brønsted acid sites does not enhance the acidity. Therefore, more active sites can be created to catalyze the conversion of ketene intermediates to light olefins, thus shifting the thermodynamically limiting step of syngas-to-ketene conversion. Under the optimized reaction conditions, a high CO conversion of 85% was obtained along with 83% light-olefin selectivity among the hydrocarbons. Notably, the light-olefin yield was as high as 48% (red circles in Figure 12a), nearly double the best values reported previously for the FTTO and OXZEO processes.

4. ELECTROCATALYTIC REACTIONS

Electrocatalysis, which involves the interconversion of chemical and electrical energy, has been gaining increasing attention in the context of carbon neutrality owing to the direct utilization of renewable energy. Professor Bao's team has applied the fundamental understanding and research methodology of thermal catalysis to the field of electrocatalysis since the 2010s. These studies cover a group of electrocatalytic reactions of great importance, such as fuel cells,[76] water electrolysis,[77] CO_2 electroreduction,[78−98] and ammonia synthesis.[99]

4.1. Electrocatalytic Reactions for the Oxygen Reduction Reaction, Hydrogen Evolution Reaction, and Oxy-

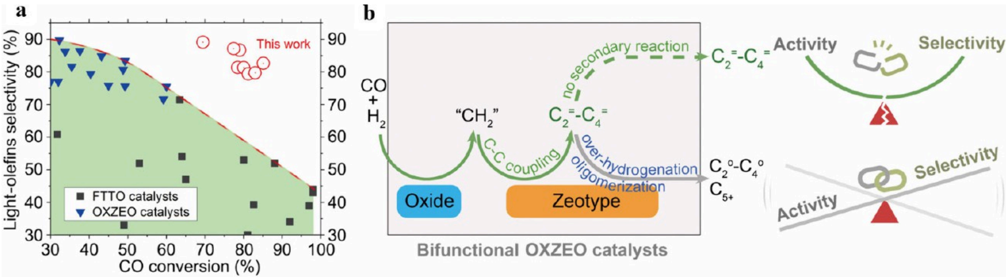

Figure 12. Activity−selectivity trade-off in the OXZEO syngas-to-light olefins process. (a) Selectivity of light olefins versus CO conversion reported for FTTO (black squares) and OXZEO (blue triangles) processes, as well as for the work under discussion (red circles). The red dashed line is an eye guide. (b) Scheme depicting the activity−selectivity trade-off caused by the entangled target and undesired secondary reactions over zeotypes.[66] Reproduced with permission from ref 66. Copyright 2023 American Association for the Advancement of Science.

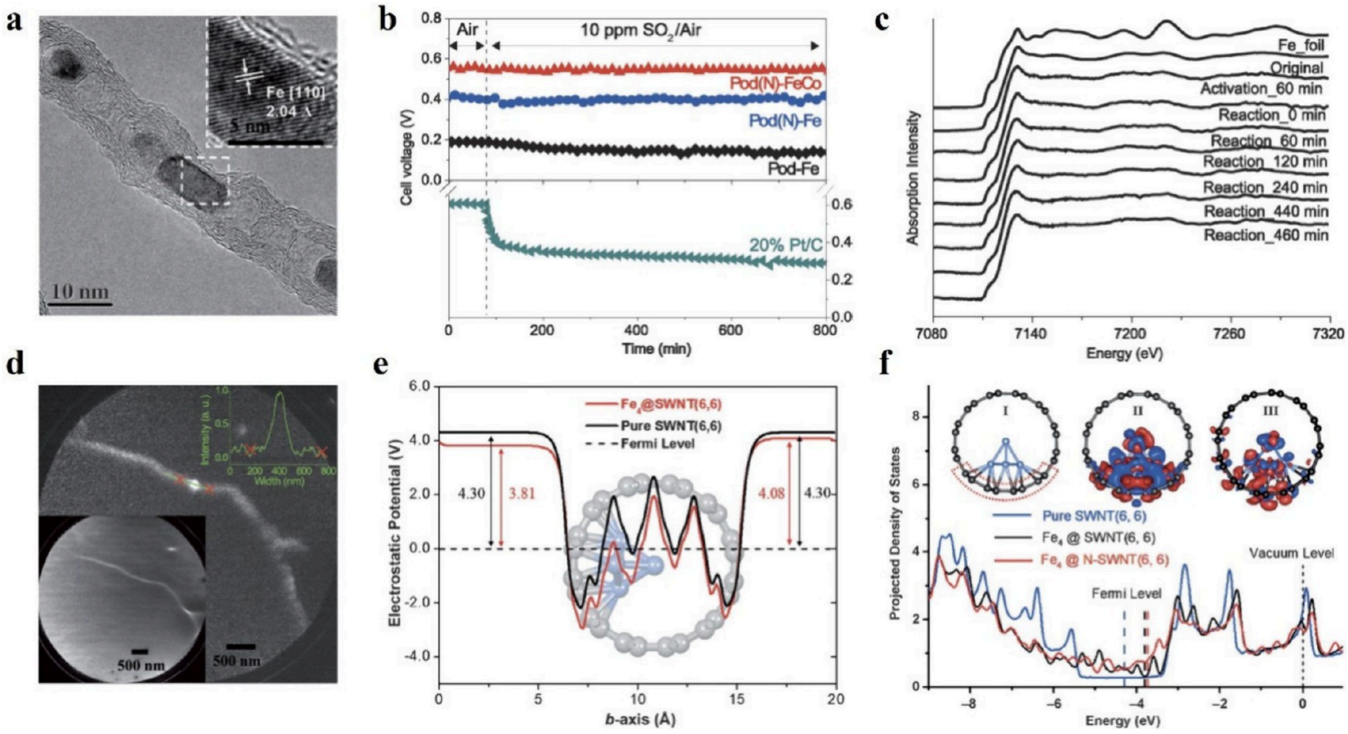

Figure 13. (a) High-resolution (HR)TEM image of Pod-Fe with the inset showing the [110] crystal plane of the Fe particle. (b) Durability tests in the presence of 10 ppm of SO$_2$ in air using the Pod-Fe, N-doped Pod-Fe (Pod(N)-Fe), and Pod(N)-FeCo cathodes, respectively, compared to 20% Pt/C with a Pt loading of 0.2 mg cm^{-2}. (c) In situ Fe K-edge XANES of the Pod-Fe cathode under proton-exchange membrane fuel cell operation conditions. (d) PEEM image of Pod-Fe acquired with an initial laser voltage of 1.7 V. The top inset displays the brightness profile along the green line, while the bottom inset shows the corresponding LEEM image of the same area. (e) Electrostatic potential profiles averaged over plane perpendicular to the *b*-axis as a function of the *b*-axis position in the supercell of Fe$_4$@SWNTs and pure SWNTs, respectively. (f) Projected density of states (DOS) of the p orbitals of C atoms bonded to Fe$_4$ in Fe$_4$@SWNT and Fe$_4$@N-SWNT compared with that in pure SWNT.[16] Reproduced with permission from ref 16. Copyright 2013 John Wiley and Sons.

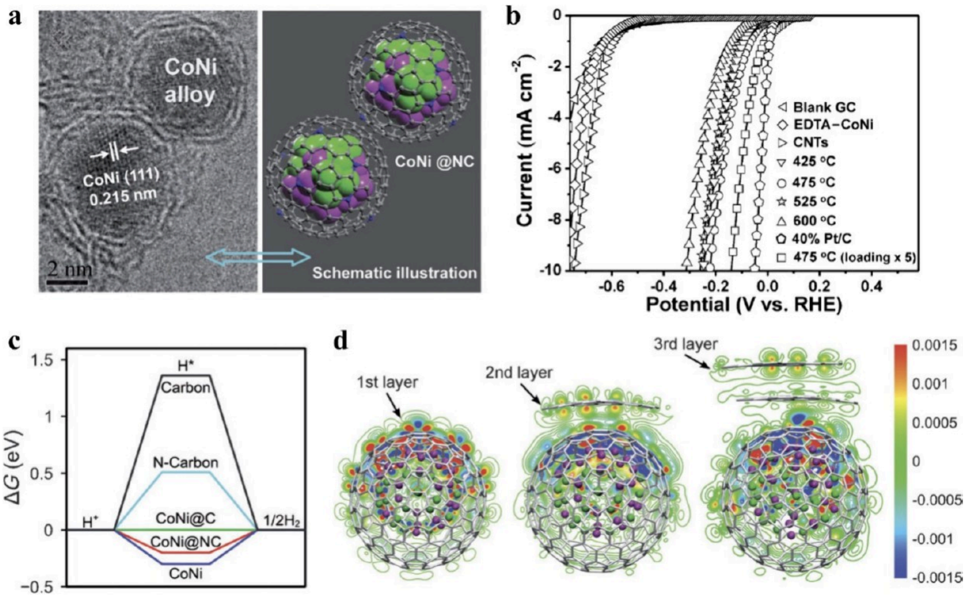

Figure 14. (a) HRTEM image of the CoNi nanoparticles encapsulated by graphene (CoNi@NC) and a schematic of the CoNi@NC structure. (b) HER polarization curves for the CoNi@NC samples prepared at different temperatures compared to the reference samples. (c) DFT-calculated HER mechanism on different catalysts. (d) Differential charge density showing the redistribution of the electrons in the CoNi@NC structures with one to three layers of graphene. The red and blue regions denote increased and decreased electron density, respectively.[100] Reproduced with permission from ref 100. Copyright 2015 John Wiley and Sons.

gen Evolution Reaction. The interconversion between hydrogen and electricity can be easily achieved using fuel cells and water electrolysis, enabling the flexible and on-demand supply of electricity and hydrogen. The oxygen reduction

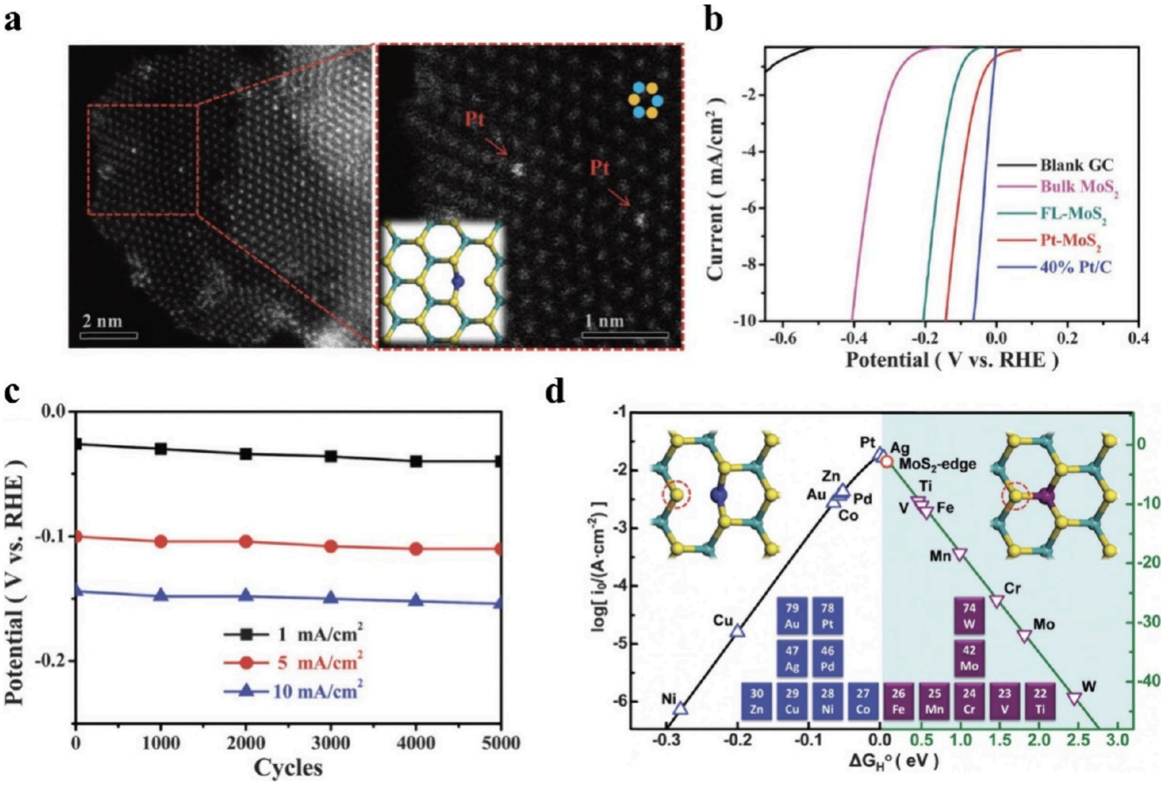

Figure 15. (a) High-angle annular dark-field imaging images of MoS_2 confining single Pt atoms in the 2D basal plane (Pt-MoS_2). (b) HER polarization curves for Pt-MoS_2 in comparison with reference catalysts. (c) Stability tests of the Pt-MoS_2 at different current densities. (d) Volcano plot of current versus hydrogen adsorption energy.[104] Reproduced with permission from ref 104. Copyright 2015 Royal Society of Chemistry.

reaction (ORR) is key in fuel cells and is restricted by the lack of active, durable, and earth-abundant catalysts.

For the ORR, a catalyst with iron nanoparticles encapsulated inside pod-like CNTs (Pod-Fe, Figure 13a) was prepared by Professor Bao's team, and it exhibited excellent electrocatalytic activity and stability for the acidic ORR, as well as good tolerance to SO_2 (10 ppm) poisoning (Figure 13b).[16] In situ X-ray absorption fine structure (EXAFS) characterization of the catalyst showed that the metallic state of the Fe nanoparticles was maintained in an acidic reaction environment during the ORR process (Figure 13c) owing to full protection by the carbon wall. Further, photoemission electron microscopy (PEEM) analysis and DFT calculations of the electronic structure of Pod-Fe revealed that the chemically inert carbon surface was activated by the encapsulated Fe via the electronic interaction between the Fe 3*d* and C 2*p* orbitals, as well as electron transfer from Fe to the carbon surface, which increased the electronic density of the C 2*p* states near the Fermi level and decreased the work function of the carbon surface (Figures 13d−f). Consequently, O_2 was efficiently activated and electroreduced to form H_2O on the modulated carbon surface. Crucially, Bao et al. reported that a spatially confined metal in the cavity of chemically and mechanically stable CNTs can significantly change the electronic structure of the carbon layer, inducing high catalytic activity on the originally inert carbon surface. These studies corroborate the spatial confinement effect in isolating and maintaining metastable states under harsh reaction conditions to achieve durable and efficient catalysis.

Subsequently, Bao et al. developed 2D-based catalysts for energy-conversion reactions. One representative catalytic material is the so-called "chainmail" catalyst, which is constructed by fully encapsulating metal nanoparticles within graphene layers, as discussed above (Figure 14).[100−102] In such a structure, the highly chemically stable graphene layer not only protects the inner metal from the corrosive reaction environment but is also activated by the inner metal through metal—carbon electronic interactions with electron transfer from the metal to the graphene surface. This structure exhibits both high stability and catalytic activity in a variety of reaction systems under harsh conditions, hence the name: the chainmail catalyst. This study provided a new approach for developing nonprecious metal catalysts.[103]

The activity and stability of chainmail catalysts depend on the thickness of the graphene layer and the type of inner metal used. To optimize the catalytic performance of chainmail catalysts, Professor Bao and co-workers developed advanced synthetic techniques to control the thickness of the graphene layer, thus realizing the controllable synthesis of the chainmail catalysts with one to three graphene layers encapsulating different metal nanoparticles. Further, these were successfully applied to many catalytic reactions, thus achieving high performance.

One significant application of chainmail catalysts is electrocatalytic water splitting for both the hydrogen evolution reaction (HER) and oxygen evolution reaction (OER). For the acidic HER, Bao's team controllably synthesized a chainmail catalyst with CoNi nanoparticles encapsulated predominantly by one- and two-layer graphene doped with nitrogen (Figure 14a), which exhibited both high stability and activity with an overpotential of only 142 mV at 10 mA cm^{-2}, comparable to that of the commercial 40% Pt/C catalyst (Figure 14b).[100] Theoretical calculations showed the synergistic effect of the CoNi metal and nitrogen dopants in improving the catalytic activity of the graphene surface via electron transfer from the metal to the surface through up to three graphene layers, which

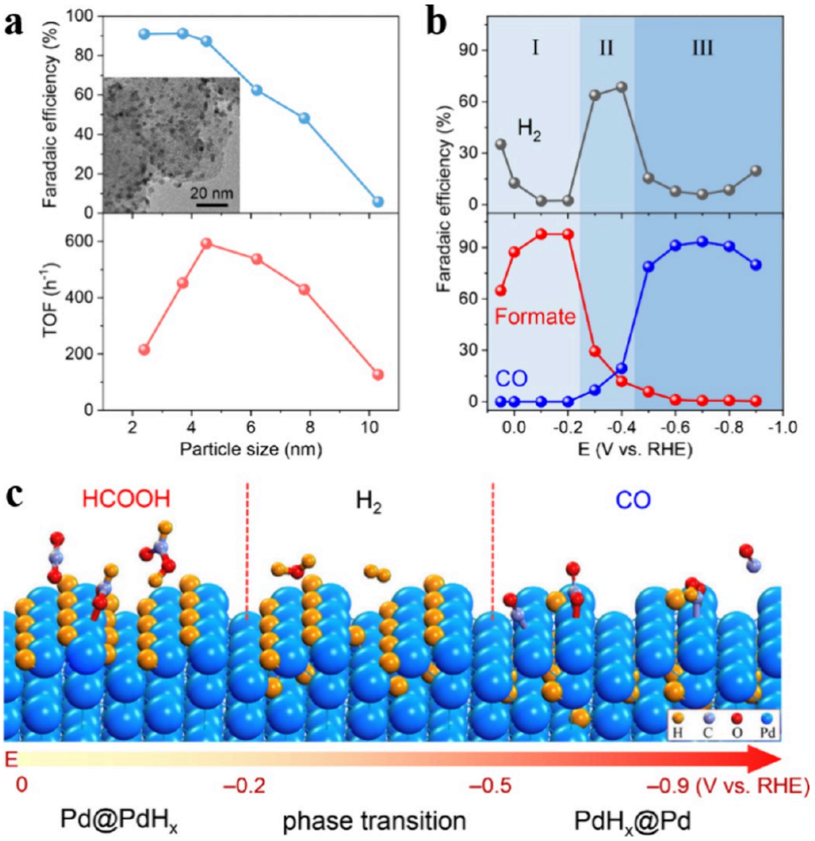

Figure 16. (a) Faradaic efficiency and TOF for CO production as a function of Pd nanoparticle size at −0.89 V vs RHE. The inset is a typical TEM image of size-selected Pd nanoparticles (3.7 nm).[78] Reproduced with permission from ref 78. Copyright 2017 American Chemical Society. (b) CO, formate, and H_2 faradaic efficiencies as a function of applied potential over 3.7 nm Pd nanoparticles. (c) Active phase structures of Pd nanoparticles in different potential windows.[79] Reproduced with permission from ref 79. Copyright 2017 Springer Nature.

notably enhanced hydrogen adsorption (Figures 14c and 14d). Concerning the OER, they further developed a unique template method for preparing chainmail catalysts using confined channels of mesoporous silica and successfully synthesized a chainmail catalyst with different metal nanoparticles encapsulated predominantly by single-layer graphene.[101] Electron transfer from the encapsulated metal to single-layer graphene efficiently regulated the electronic structure of graphene, thereby inducing excellent OER activity on the inert carbon surface. They showed that the CoNi@graphene catalyst delivered the best OER activity, having an overpotential of only 280 mV at 10 mA cm^{-2} in alkaline solutions and exhibiting a high durability of 10000 cycles, both of which exceed those of the commercial IrO_2 catalyst.

Another representative category of catalysts developed by Bao et al. is 2D catalytic materials with heteroatoms confined in the crystal lattice. Stable 2D materials such as graphene and MoS_2 typically have chemically inert open surfaces that are not catalytically active. Bao showed that by confining metal heteroatoms into a 2D lattice to create low-coordinated metal sites with unique electronic states, an inert surface can be effectively activated to induce high catalytic activity for a variety of reactions.[29,104,105]

One example is a graphene-encapsulated Cu(I)−N (Cu−N©C) catalyst with highly exposed and coordinatively unsaturated Cu(I)−N active sites prepared by the facile pyrolysis of commercially available Cu phthalocyanine and dicyandiamide.[76] Apart from acting as an electron-conducting path, the graphene matrix stabilized the high density of Cu(I)−N active sites with a high Cu loading of up to 8.5 wt %. The Cu−N©C catalyst showed impressive activity and stability for the ORR, even with an ultralow catalyst loading. However, efficient hydrogen production via water electrolysis driven by renewable electricity is also highly desired. The team reported a bifunctional, nonprecise metal catalyst for water electrolysis, namely Co nanoparticles encapsulated in nitrogen-doped carbon (Co@N−C). The Co@N−C catalyst exhibited high activity and excellent stability for both the HER and OER in alkaline media.[77]

Another example is metal-heteroatom-doped MoS_2. Bao et al. first reported that by confining Pt atoms in the lattice of MoS_2, the HER activity was remarkably improved compared with that of pure MoS_2 and could be stably maintained for 5000 cyclic voltammetry (CV) sweeps (Figures 15a−c).[104] This high activity was attributed to the activation of in-plane S sites by neighboring Pt atoms confined in the lattice. Based on DFT calculations, the optimum metal dopants were screened based on the relationship between the hydrogen adsorption energy and HER activity (Figure 15d). Thus, Bao et al. provided an effective approach for stimulating and modulating the catalytic activity of MoS_2 for the HER.

4.2. Electrocatalytic CO_2 Reduction to Valuable Chemicals and Fuels. In the past decade, the number of studies on electrocatalytic CO_2 reduction to valuable chemicals and fuels (e.g., CO, formate, methane, ethylene, ethanol, acetate, and *n*-propanol) using nanostructured heterogeneous metal catalysts at ambient temperature and pressure has increased rapidly. By preparing size-selected Pd nanoparticles, an HER-

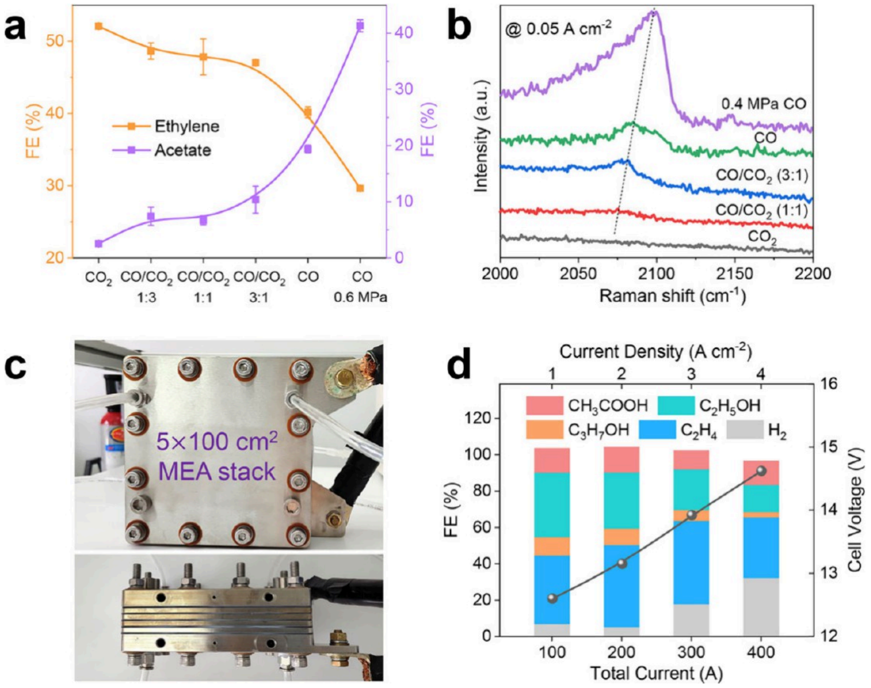

Figure 17. (a) Faradaic efficiencies of ethylene and acetate and (b) operando $^*CO_{atop}$ Raman peaks over a CuO nanosheet catalyst. (c) Photographs of an electrolyzer stack with five 100 cm^2 MEAs and (d) corresponding CO electrolysis performance.[88] Reproduced with permission from ref 88. Copyright 2024 Springer Nature.

active bulk Pd electrode can be converted into a catalyst that is selective for CO_2 electroreduction.[78] Notably, the CO faradaic efficiency over Pd nanoparticles increased with the decrease in particle size at −0.89 V vs the reversible hydrogen electrode (RHE), whereas the turnover frequency (TOF) for CO production exhibited a volcano-type relationship with particle size (Figure 16a). This size dependence is clearly different from those of other metals such as Au and Ag. Using 3.7 nm Pd nanoparticles as a model catalyst, the potential-dependent variations in the product selectivity and active phase were revealed.[79] The faradaic efficiencies of both CO and formate exceeded 90% in the different potential windows. This selectivity switch can be rationalized by the potential- and intermediate-induced active phase transitions (from $Pd@PdH_x$ to $PdH_x@Pd$) under the reaction conditions (Figures 16b and 16c). The Pd nanoparticles also show improved CO_2 hydrogenation with H_2 to produce formate owing to the shared HCOO* intermediate during both thermocatalytic and electrocatalytic CO_2 reduction.[81] This is a new example of the electrochemical promotion of catalysis (EPOC) effect in low-temperature aqueous electrocatalytic and coupled thermocatalytic and electrocatalytic reactions. Motivated by the concept of nanoconfinement catalysis, Au(Ag)−CeO_x catalysts with abundant metal−oxide interfaces were used for CO_2 electroreduction. These interfaces facilitate CO_2 adsorption and hydrogenation to the initial *COO and *COOH intermediates, resulting in improved CO production compared with bare Au and Ag.[80] Metal- and nitrogen-doped carbon materials with metal−nitrogen (M−N) motifs constitute a new class of single-atom electrocatalysts. For example, a Ni−N−C catalyst with a high Ni loading of 5.44 wt % achieved a high CO current density of 71.5 mA cm^{-2} and a TOF of 10,087 h^{-1} for CO production in an H-cell.[82] The CUS Ni−N sites are unfavorable for the competing HER but favorable for CO desorption owing to weakened *CO adsorption compared with that of bulk Ni nanoparticles. Such a Ni−N−C catalyst also exhibited promising CO_2 electroreduction performance in acidic media.[87]

Beyond catalysts, an efficient and practical CO_2 electrolyzer should be operated at industrial current densities (>200 mA cm^{-2}), which can be achieved using a gas diffusion electrode (GDE) configuration that reduces the diffusion pathway of CO_2 by 2 to 3 orders of magnitude.[84] Recent studies by Professor Bao's team focused on developing practical CO_2/CO electrolysis routes through efforts in fundamental catalysis and electrolysis technologies. By incorporating a Cu−CuI powder catalyst into a gas diffusion electrode (GDE) in a flow cell, the partial current density for multicarbon (C_{2+}) products reached 591 mA cm^{-2} at −1.0 V vs RHE.[85] The conversion efficiency from electrical to chemical energy was further increased by developing zero-gap membrane electrode assembly (MEA) electrolyzers. By adjusting the feed composition in an alkaline MEA electrolyzer, a selectivity switch from ethylene to acetate with increasing CO pressure in the feed is induced by increasing *CO coverage and the local pH in the reaction microenvironments (Figures 17a and 17b).[86] Notably, with a grain boundary-rich Cu nanoparticle catalyst, the C_{2+} partial current density reached as high as 4.35 A cm^{-2} and the full-cell energy efficiency reached up to 40% for CO electrolysis to C_{2+} products.[88] Further, an electrolyzer stack with five 100 cm^2 MEAs was assembled and achieved stable CO electrolysis at a high current of 400 A (Figures 17c and 17d). Two strategies to address the CO_2 crossover issue in alkaline CO_2 electrolysis have been proposed, namely, tandem acidic CO_2 electrolysis to CO, followed by alkaline CO electrolysis to C_{2+}, and direct acidic CO_2 electrolysis to C_{2+} products.[87]

Solid oxide electrolysis cells (SOECs) can convert surplus electricity from clean primary energy sources (e.g., solar, wind, and geothermal) and waste heat from nuclear reactors or industry into stable chemical energy by directly electrolyzing CO_2 to CO. Such processes are essential for clean energy storage and the development of carbon-centered energy cycles for reducing our carbon footprint.[89] During CO_2 electrolysis in an SOEC, CO_2 is electroreduced to CO and O^{2-} (CO_2RR, $CO_2 + 2e^- = CO + O^{2-}$) at the cathode, and O^{2-} is transported through the electrolyte to the anode, generating O_2 via the OER ($2O^{2-} - 4e^- = O_2$).[106] Because the cathodic CO_2RR is a two-electron transfer process, whereas the anodic OER is a four-electron transfer process, the OER is kinetically sluggish, especially at intermediate temperatures (i.e., <700 °C). Therefore, developing advanced anode materials is critical for accelerating the OER kinetics and improving SOEC performance.

Perovskite oxides are widely used as anodes for SOECs. Therefore, optimizing the electronic structure of perovskite anode materials is an efficient strategy to improve OER activity and stability.[107] For $Ca_xSr_{1-x}Co_{0.7}Fe_{0.3}O_{3-\delta}$ (x = 0, 0.5, and 1), the A-site-induced structural transformation from orthorhombic brownmillerite $CaCo_{0.7}Fe_{0.3}O_{3-\delta}$ to tetragonal perovskite $SrCo_{0.7}Fe_{0.3}O_{3-\delta}$ raises the O 2p-band center to the Fermi level. This enhances M 3d−O 2p orbital hybridization and increases the oxygen vacancy concentration, boosts oxygen ion migration capacity, and improves electrical conductivity. At 800 °C, an SOEC with the $SrCo_{0.7}Fe_{0.3}O_{3-\delta}$ anode achieved the current density of 2.03 A cm^{-2} at 1.6 V and demonstrated stable operation for 487 h at 1.2 V. This performance surpasses that of benchmark anodes such as $La_{0.6}Sr_{0.4}Co_{0.2}Fe_{0.8}O_{3-\delta}$, $Ba_{0.5}Sr_{0.5}Co_{0.8}Fe_{0.2}O_{3-\delta}$, and $PrBaCo_2O_{6-\delta}$.[108]

Furthermore, the ordering of A-site cations and oxygen vacancies in double perovskite oxides significantly affects the distribution of oxygen vacancies and the mobility of oxygen ions within the perovskite crystal structure. This, in turn, affects the high-temperature OER performance. However, these effects are complex and remain largely unexamined and poorly understood. To understand these processes better, Professor Bao's team fabricated a series of $PrBaCo_{2-x}Fe_xO_{5+\delta}$ perovskites with tailored ion ordering and revealed that the oxygen bulk migration and OER activities were enhanced by the A-site cation ordering but weakened by oxygen vacancy ordering. Hence, SOECs with A-site-ordered and oxygen-vacancy-disordered $PrBaCo_2O_{5+\delta}$ anodes display the highest performance of 3.40 A cm^{-2} at 800 °C and 2.0 V.[91]

However, for the perovskite anode, the formation of cation-enriched secondary phases at the surface might block the active sites and decrease the OER performance.[109] To address this problem, Bao et al. infiltrated Au nanoparticles into a yttria-stabilized zirconia (YSZ) scaffold and demonstrated that the Au/YSZ interface possesses excellent OER performance in an SOEC for CO_2 electrolysis. The current density for the Au/YSZ-7.7 anode reached 1.39 A cm^{-2} at 1.4 V and 800 °C, which is much higher than those conventional perovskite anodes. Electrochemical characterization, DFT calculations, and in situ XPS results revealed that Au particles can significantly promote interfacial oxygen spillover from the YSZ to the Au surface and accelerate the OER process under anodic polarization. This study provides an alternative perspective for understanding the OER mechanism at high temperatures, which may be useful for exploring efficient anode materials.[110]

Recently, C_xH_y-assisted SOECs have attracted great interest because of their ability to decrease the energy demand for CO_2 electrolysis by feeding low-cost and abundant C_xH_y to the anode of the SOEC and replacing the OER with the C_xH_y electrooxidation reaction, which is more thermodynamically favorable.[111] The consumption of oxygen species by the fed C_xH_y remarkably reduced the anodic oxygen partial pressure and lowered the open circuit voltage (OCV) of the SOEC, leading to accelerated anode reaction kinetics and enhanced CO_2 electrolysis. Furthermore, by optimizing the surface electronic structure and components of the anode, the total oxidation of C_xH_y could be efficiently inhibited, enabling the selective conversion of C_xH_y into value-added chemicals instead of CO_2 and H_2O, which makes C_xH_y-assisted SOECs more economically attractive.

An in situ exsolution strategy has been applied to fabricate stable CoFe alloy nanoparticles on the surface of an $La_{0.6}Sr_{0.4}Ti_{0.3}Fe_{0.5}Co_{0.2}O_{3-\delta}$ anode for a CH_4-assisted SOEC, and the device showed superior anodic partial oxidation of methane (POM) performance (Figure 18a). The electrical energy consumption for CO decreased from 3.46 kWh m^{-3} in the conventional SOEC to 0.31 kWh m^{-3} in the CH_4-assisted SOEC (Figure 18b). Further, the CH_4 conversion reached 86.9% with a CO selectivity of up to 90.1%. Moreover, stable operation for over 1250 h with a CO selectivity above 95% was possible at 800 °C (Figure 18c). Thus, the C_xH_y-assisted SOEC provides an efficient strategy to boost the cathodic CO_2 electroreduction performance thermodynamically and simultaneously convert C_xH_y to value-added chemicals at the anode.[94]

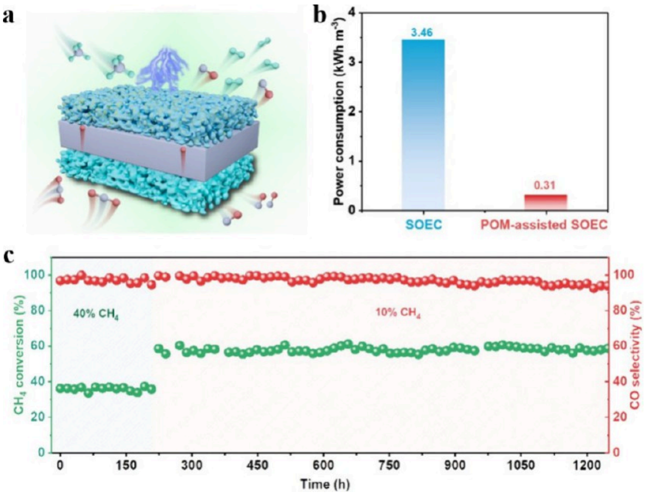

Figure 18. (a) Schematic of POM-assisted SOEC. (b) Electricity consumption of conventional SOEC and POM-assisted SOEC at 800 °C. (c) Stability tests of LSTFC2-R for the anodic POM reaction.[94] Reproduced from ref 94. Copyright 2024 Cell Press.

In addition to the anodic reactions, cathodic CO_2 adsorption and activation are essential for high-temperature CO_2 electrolysis in SOECs. To achieve this, the in situ exsolution of metal nanoparticles in perovskites under a reducing atmosphere has been employed to construct an active metal−oxide interface for CO_2 electrolysis. Doping Mo atoms at the B sites of $La_{0.4}Sr_{0.6}Co_{0.2}Fe_{0.7}Mo_{0.1}O_{3-\delta}$ (LSCFM) increases the segregation energy of Co and Fe ions and improves the exsolution of CoFe alloy nanoparticles. Further, the metal−oxide interface improved the CO_2 adsorption and activation, showing improved CO_2 electrolysis performance compared to its LSCFM counterparts.[95] Moreover, in situ X-ray diffraction, scanning transmission electron microscopy, environmental scanning electron microscopy, and DFT calculations were carried out to investigate the reversible exsolution and dissolution of CoFe alloy nanoparticles in Co-doped $Sr_2Fe_{1.5}Mo_{0.5}O_{6-\delta}$ (SFMC) double perovskites. Under a reducing atmosphere, the facile exsolution of Co facilitates the

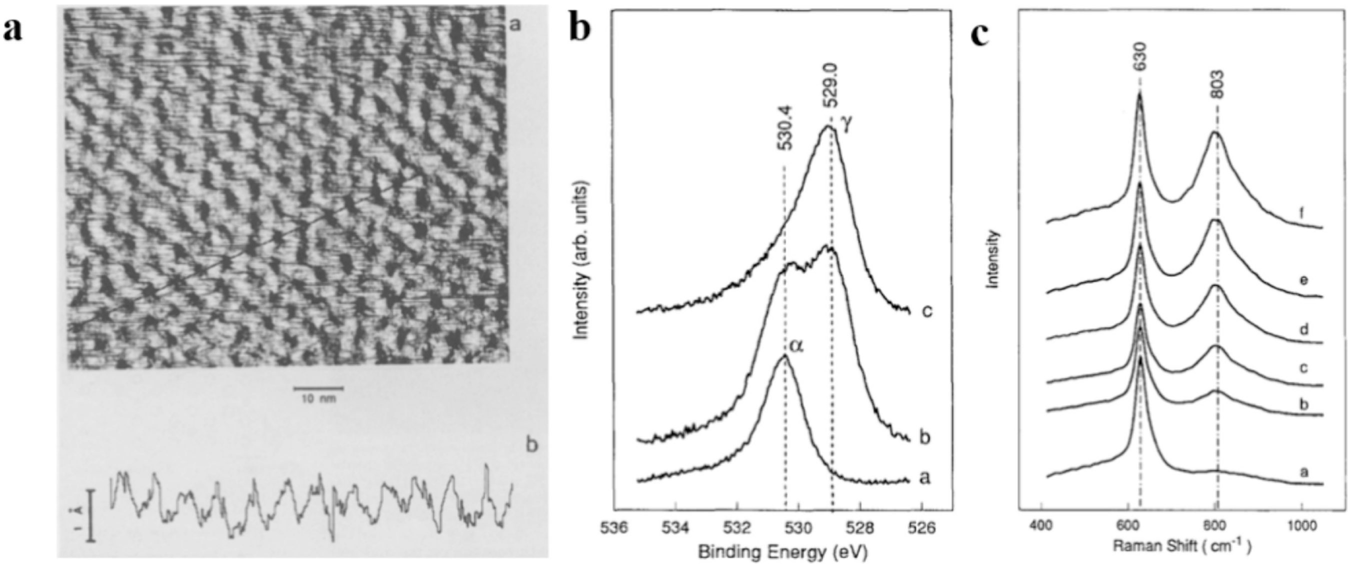

Figure 19. Tuning the catalytic behavior using metallic Ag with subsurface O. (a) STM image (900 × 900 Å) of the reconstructed Ag(111) surface, formed after exposing the bulk Ag(111) crystal to 1 bar O_2 at 900 K for 400 h, along with the corrugated profile along the specified line.[113] Reproduced with permission from ref 113. Copyright 1993 Elsevier. (b) O 1s XPS data from the Ag(111) surface after exposure to 1 bar O_2: (line a) at 450 K for 5 h; (line b) at 780 K for 1 h; and (line c) at 780 K for 7 h. (c) Raman spectra monitoring the formation of O species on and near a faceted Ag(110) surface previously treated with O_2 at high temperatures: (line a) after heating in N_2 at 900 K for 30 min; (line b to f) after exposure to 0.2 bar O_2 at 780 K for 2, 8, 15, 20, and 30 min, respectively.[115] Reproduced with permission from ref 115. Copyright 1993 Springer Nature.

reduction of Fe cations, leading to the formation of CoFe alloy nanoparticles in the SFMC. This process is accompanied by a structural transformation from double perovskite to layered perovskite at 800 °C. Electrochemically, the CO_2 electrolysis performance can be maintained over 12 redox cycles due to the regenerative capability of the CoFe alloy nanoparticles. Anchoring these CoFe alloy nanoparticles within the SFMC perovskite through reduction not only enhances CO_2 electrolysis performance but also improves stability compared to the pristine SFMC perovskite.[96] However, obtaining abundant metal/oxide interfaces poses significant challenges due to the slow diffusion of dopant cations within bulk perovskites. To address this, Bao et al. developed a strategy to promote the exsolution of RuFe alloy nanoparticles on $Sr_2Fe_{1.4}Ru_{0.1}Mo_{0.5}O_{6-\delta}$ perovskite by enriching active Ru beneath the perovskite surface through repeated redox manipulation. In situ scanning transmission electron microscopy revealed the dynamic structural evolution of $Sr_2Fe_{1.4}Ru_{0.1}Mo_{0.5}O_{6-\delta}$ under reducing and oxidizing atmospheres, as well as enhanced CO_2 adsorption at the RuFe@$Sr_2Fe_{1.4}Ru_{0.1}Mo_{0.5}O_{6-\delta}$ interfaces. Further, SOECs with RuFe@$Sr_2Fe_{1.4}Ru_{0.1}Mo_{0.5}O_{6-\delta}$ interfaces showed more than 74.6% enhancement in the current density for CO_2 electrolysis compared to that with $Sr_2Fe_{1.4}Ru_{0.1}Mo_{0.5}O_{6-\delta}$ counterpart, as well as impressive stability over 1000 h at 1.2 V and 800 °C.[112]

In addition to the active exsolved nanoparticles, Bao et al. also anchored stable single Ru atoms on the surface of an oxygen ionic conductor ($Ce_{0.8}Sm_{0.2}O_{2-\delta}$, SDC) via a strong covalent metal–support interaction. This interaction significantly modified the electronic structure of the SDC surface, promoting oxygen vacancy formation and enhancing CO_2 adsorption and activation. Consequently, the electrocatalytic activity of SDC for high-temperature CO_2 electrolysis was greatly improved. Experimentally, an SOEC with the Ru1/SDC-$La_{0.6}Sr_{0.4}Co_{0.2}Fe_{0.8}O_{3-\delta}$ cathode shows a current density as high as 2.39 A cm^{-2} at 1.6 V and 800 °C. Overall, that study expanded the application of single-atom catalysts to high-temperature electrocatalytic reactions in SOECs and offered an effective strategy for precisely tailoring the electronic structure and electrocatalytic activity of SOEC cathodes at the atomic level.[98]

5. DEVELOPMENT OF SURFACE SCIENCE CONCEPTS AND CATALYTIC CHARACTERIZATION METHODS

For the characterization of heterogeneous catalytic reactions, noninvasive measurements of the active sites, reaction mechanisms, and kinetics inside the reactor under realistic reaction conditions are necessary but challenging. Therefore, Professor Bao's team has devoted itself to developing advanced characterization techniques and methods, including surface analytical techniques and NMR.

5.1. Observation of Subsurface Oxygen Species with Multiple Surface Science Techniques.

Most metal surfaces, particularly group IB metals such as silver and gold, interact only weakly with oxygen molecules and therefore have limited capacity to adsorb and dissociate oxygen molecules to form surface-active oxygen species. This interaction is typically essential for subsequent catalytic oxidation reactions. Nonetheless, these metals often act as highly selective oxidation catalysts, presenting a contrast to the conventional understanding that catalytic reactions must proceed through distinct "adsorption–activation–reaction" stages. This contradiction poses a significant scientific challenge in heterogeneous catalysis. Since the 1990s, Bao and Ertl have studied the activation of molecular oxygen over a model metallic Ag(111) surface. They observed that oxygen promoted the reconstruction of the Ag(111) surface at high temperatures (Figure 19a).[113] The corresponding XPS O 1s spectra show a new signal at a binding energy of 529 eV (Figure 19b).[114] Further, in situ Raman spectroscopy revealed a strong signal in the vibrational mode at 803 cm^{-1} (Figure 19c).[115] These results demonstrate the presence of new atomic oxygen species on the reconstructed Ag(111) surface. Angle-

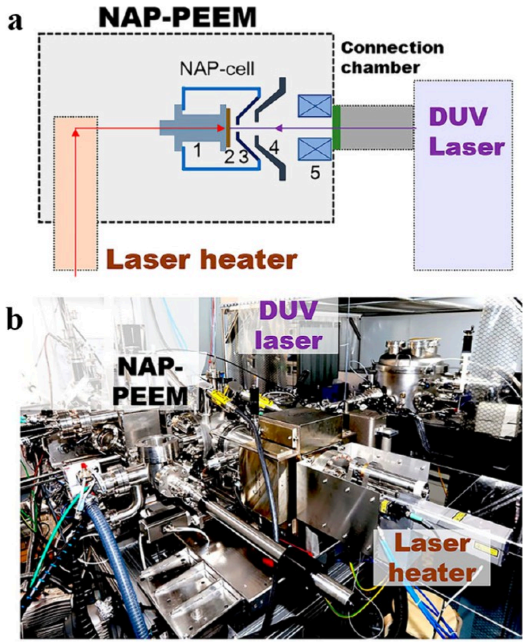

Figure 20. (a) Schematic illustration of the experimental setup, depicting the relative positions of the DUV laser, NAP-PEEM system, and laser heater. Key components include: (1) sample cartridge (gray); (2) sample (brown); (3) nozzle (blue); (4) objective lens electrodes (black); and (5) electron beam deflector (light blue). The green rectangle in the connection chamber represents a CaF_2 window. The DUV laser (indicated by the purple line) is directed normally onto the sample surface. The heating IR laser (represented by the red line) is aligned with the sample cartridge to heat the sample from the backside. (b) Photograph of the DUV-NAP-PEEM system.

dependent XPS and highly surface-sensitive ion scattering spectroscopy (ISS) experiments further indicated that the oxygen species were localized on the silver subsurface.[116] The presence of subsurface oxygen promotes the adsorption of molecular oxygen and other C_1 molecules on the Ag surface, which greatly increases the activity of CO oxidation and selective methanol oxidation to formaldehyde. In addition, the adsorbed surface oxygen species induced by the subsurface oxygen enabled the partial oxidation of methanol to formaldehyde with high selectivity without overoxidation, producing undesired CO_2.[117]

5.2. Development of Photoemission Electron Microscope.

PEEM is a potent surface analysis technique that enables in situ investigation of dynamic surface processes in real space. It has found extensive application in examining the chemical, magnetic, and electronic properties of solid surfaces across fields such as surface science, catalysis, materials science, and biology. Professor Bao has used this technique to investigate dynamic surface processes since the 1990s; however, the performance of the PEEM setup requires improvement.[118−135] The advancement of PEEM instruments heavily depends on utilizing state-of-the-art light sources and enhanced electron optics.

Professor Bao et al. first applied a deep ultraviolet (DUV) light source to PEEM (Figure 20). Leveraging the high energy and power of DUV, the PEEM system achieved a spatial resolution of 3.9 nm, which is the best in the world, and an energy resolution of 0.102 eV. This system has been successfully applied to in situ and dynamic studies in catalysis, materials science, and energy fields. Moreover, developing near-ambient pressure PEEM systems that can image surface chemistry across a wide range of gas pressures, from UHV to high pressures, presents significant challenges. In PEEM, a high electric field—typically on the order of 10^7 V/m—is created between the sample and the objective lens (anode) by applying high voltages, such as 20 kV, between the sample (cathode) and the objective lens (anode). Imaging with cathode lenses in the presence of high-pressure gases at the sample surface poses significant challenges due to potential gas discharge, scattering of low-energy electrons by molecules, and instability of the sample. Bao's team has made continuous efforts to address these problems. A two-stage accelerating electric field has been designed, featuring a low-field region between the sample and the intermediate electrode ("nozzle"), and a high-field region between the nozzle and the objective lens. Additionally, a three-stage differential pumping system enables the establishment of a near-ambient-pressure environment at the sample surface. Furthermore, a near-ambient-pressure (NAP) cell has been constructed to maintain the sample in a high-pressure gaseous atmosphere. High-resolution PEEM imaging was successfully demonstrated on solid surfaces in gas environments at pressures up to 1 mbar.

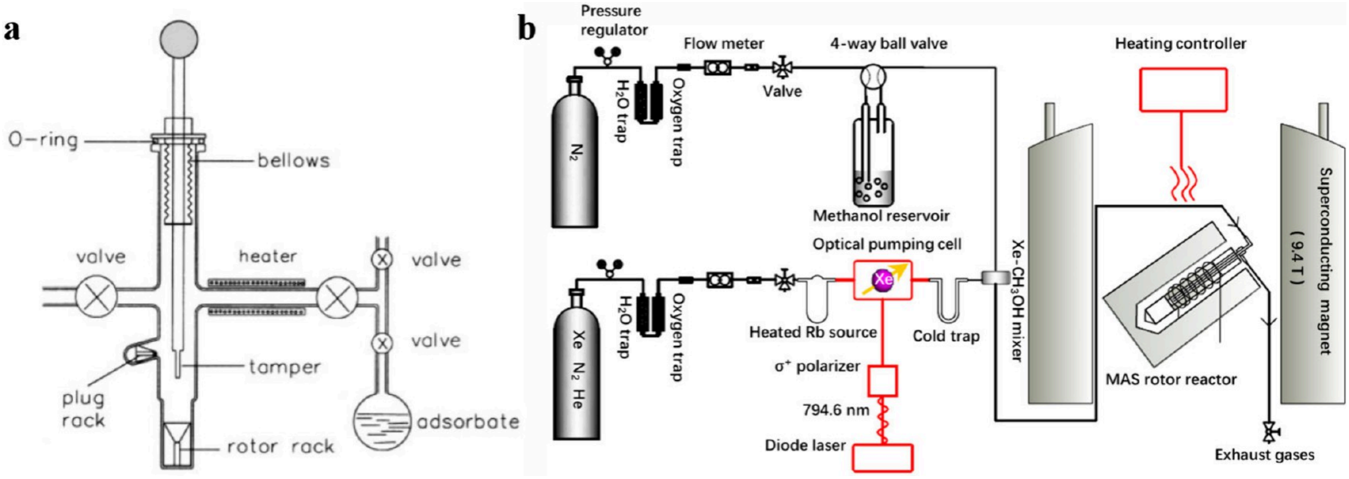

Figure 21. (a) Diagram of the evacuation, loading, and sealing of solid samples for MAS NMR studies under batch-like condition.[137] Adapted with permission from ref 137. Copyright 1999 Royal Society of Chemistry. (b) Sketch of the experimental setup for in situ MAS NMR coupled with hyperpolarized ^{129}Xe under continuous-flow conditions.[138] Reproduced with permission from ref 138. Copyright 2009 American Chemical Society.

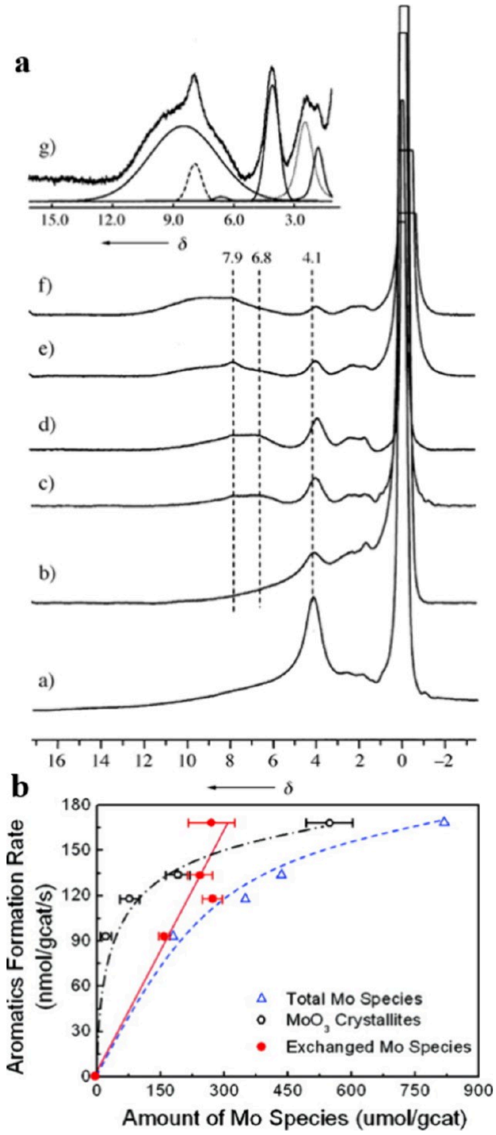

Figure 22. (a) In situ ^{1}H MAS NMR spectra of 6 wt % Mo/HZSM-5 catalyst after treated with (a) methane flow at 873 K for 1 h. (b)−(f) After the MDA reaction under 973 K, 1500 mL g^{-1} h^{-1}, 1 atm. Reaction times: (b) 10 min, (c) 30 min, (d) 1h, (e) 3 h, and (f) 6 h. Inset spectrum (g) indicates the expansion of spectrum (e), with six lines simulating the original spectrum.[139] Adapted with permission from ref 139. Copyright 2000 John Wiley and Sons. (b) Correlation of the aromatic formation rate with different molybdenum species.[141] Reproduced with permission from ref 141. Copyright 2008 American Chemical Society.

5.3. Development of in Situ/Operando Solid-State NMR Techniques. In situ solid-state NMR is a well-established tool for investigating the structures of adsorbed reactants, intermediates, and products on the surface of solid catalysts. These techniques allow the identification of catalytic sites, such as the coordination state of atoms, acidic sites, and dynamics of reaction processes, after the introduction of adsorbates and reactants inside an NMR rotor under magic angle spinning (MAS).[136]

As shown in Figure 21, Bao proposed two NMR experimental methods for in situ research, in which catalytic reactor conditions were simulated in an NMR rotor under batch-like or continuous-flow conditions, respectively.[137,138] The batch-like processing mode is a simple method that requires processing of the sample before activation (dehydration) and adsorption with the adsorbate in the NMR probe. To reproduce the catalytic reaction conditions in an environment suitable for NMR spectroscopy, Bao et al. designed a special device, as shown in Figure 21a, for the online processing of powder samples.[137,139] Using this system, solid samples can be heated to approximately 1000 K under vacuum for dehydration and exposed to several different gases in parallel or separately, according to the adsorption and reaction requirements. After treatment, the sample was added to the NMR rotor, sealed, and transferred to a spectrometer without exposure to air. The most significant advantage is that there is no need to process the active catalyst in a glovebox for transfer to the MAS rotor. Therefore, sample preparation is substantially simplified and accelerated. Using this method, the acidity characterization of molecular sieves,[137,140] reaction process tracking of methane dehydroaromatization (MDA),[139] and CNT-confined catalysis[18] have been achieved, providing a deep understanding of the catalyst structure and reaction mechanism at the atomic or molecular scale. Taking the MDA reaction as an example, Bao's work on the application of solid-state NMR can be summarized as follows: a) the interaction between Mo species and the zeolite support; b) study of catalytic processes; and c) direct observation of active sites through ultrahigh-field ^{95}Mo NMR.[37,139−141] Using ^{1}H MAS and ^{1}H/^{27}Al transfer of population in double resonance (TRAPDOR) NMR techniques, they found condensation/reaction between Mo species and Brönsted acidic sites or extra-framework Al−OH species.[37] Combining DFT calculations and multiple-quantum (MQ) MAS NMR measurements, it was shown that a portion of the Mo species is directly bonded to the zeolite framework Al species, which is the reason for the initial conversion of reactants in the MDA reaction. Other framework Al atoms that exhibit inert adsorption toward Mo still bind to protons, maintaining their Brönsted acid properties and participating in subsequent catalytic reactions.[142] Therefore, bifunctional Mo/zeolite catalysts are generally accepted as MDA catalysts. The Brönsted acidic sites on the support play a crucial role in this reaction. Utilizing a specially designed of in situ MAS NMR apparatus (Figure 21a) that replicates the conditions of real catalytic processes, we were able to obtain ^{1}H MAS NMR spectroscopic data on the dynamic changes in proton signals from a Mo/HZSM-5 catalyst during the MDA reaction, providing insights into the catalytic MDA process in real time.[139] As shown in Figure 22a, the changes in the amount of Brönsted acidic sites during the real high-temperature reaction process at 973 K were directly observed through in situ ^{1}H MAS NMR spectroscopy, as well as the formation of water, benzene, and aromatic carbonaceous deposits during the reaction process. As the reaction evolved, the Brönsted acid signal sharply decreased at 4.1 ppm, and two new resonances appeared at 6.8 and 7.9 ppm, respectively, attributed to water and aromatic species, indicating that the Brönsted acid site is involved in aromatization or hydrogen transfer. The reaction process is stable within 1 h (Figure 22a−d). After another 2 h of reaction, the amount of aromatic species increased and presented a wider form, while the amount of adsorbed water greatly decreased (Figure 22a−e). The clearer ^{1}H MAS NMR profile of Figure 22a−e can be found in Figure 22a−g, which displays the enlarged spectrum and simulated lines. The broad signal likely originates from aromatic carbonaceous deposits on the catalyst surface. The extensive line width indicates a mixed composition and complex properties.

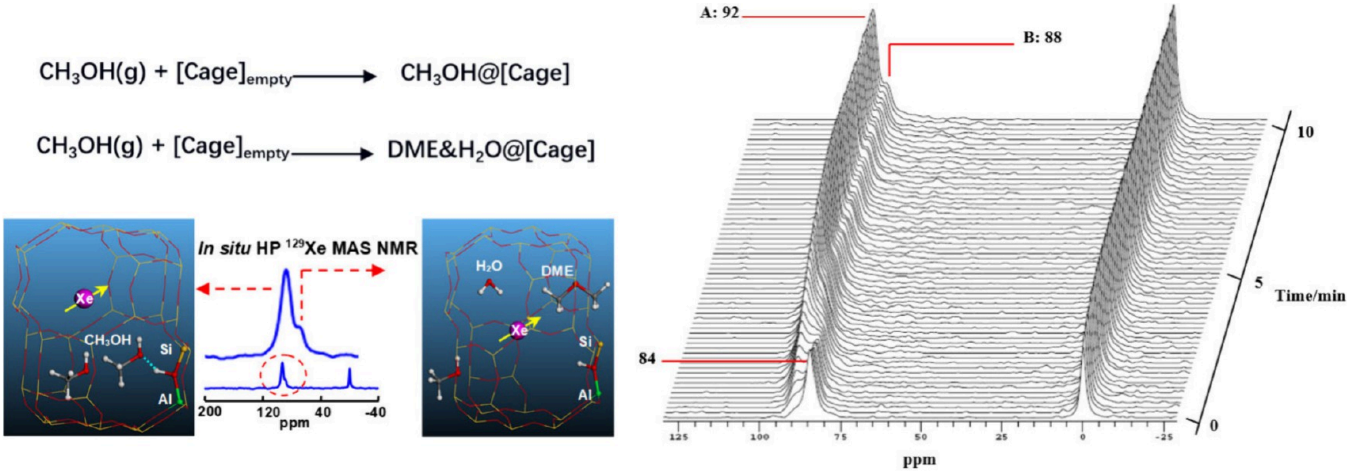

Figure 23. In situ hyperpolarized ^{129}Xe MAS NMR spectra recorded with time resolution of 10 s per spectrum as a function of time during methanol reaction in CHA nanocages at 453 K.[138] Reproduced with permission from ref 138. Copyright 2009 American Chemical Society.

These observations strongly support the acid-induced aromatization mechanism.[139] To clarify whether the active Mo species were small crystallites or isolated exchanged species, Professor Bao collaborated with Dr. Jianzhi Hu from the Pacific Northwest National Laboratory (PNNL) to analyze the Mo species using ultrahigh-field ^{95}Mo NMR spectroscopy.[141] Figure 22b shows the good correlation between the amount of Mo species exchanged and the rate of aromatic hydrocarbon formation. This indicates that the carburized molybdenum species derived from the exchanged molybdenum species were the active centers of the MDA reaction.

Because most industrial processes based on heterogeneous catalysis are typically flow processes, it has long been recognized that developing an in situ/operando flow reactor is a valuable technical goal. However, installing a MAS line in a flow reactor is challenging because it requires rotating the reactor at a speed of at least a few kilohertz while allowing the reactant gas to flow through the sample and maintain its environmental integrity. In 2009, Professor Bao's team reported a solid-state NMR probe based on a modified commercial Varian 7.5 mm NMR probe to achieve continuous flow conditions for NMR tests (Figure 21b).[138] When combined with hyperpolarized ^{129}Xe (HP ^{129}Xe) technology, this probe can increase the sensitivity of the ^{129}Xe NMR signal by four to 5 orders of magnitude, which reduces the NMR acquisition time from hours to seconds. The dynamic and kinetic processes of methanol adsorption and its reaction with dimethyl ether (DME) within the CHA nanocages were studied using hyperpolarized (HP) ^{129}Xe MAS NMR and ^{13}C MAS NMR (Figure 23). The combination of HP ^{129}Xe and ^{13}C MAS NMR distinguished the "adsorption zone" and "reaction zone" during the reaction process, and the kinetic curves and apparent activation energy of the nanocages, which involve the active site, were also quantitatively obtained. In addition, this joint technology can be extended to other nanoporous material systems: for example, (1) the role of water in methane adsorption and desorption processes in silicon-based nanochannels, and (2) a comparative study of methanol adsorption kinetics in carbon-based nanomaterials, CNTs, and silicon-based nanomaterials, MCM-41.[143,144] In the first work, HP ^{129}Xe NMR revealed the influence of pore size. For microporous one-dimensional pore structure molecular sieve ZSM-22 and mesoporous MCM-41 samples, water had a stronger inhibitory effect on methane adsorption. For the large-mesoporous SBA-15 samples, the inhibitory effect was relatively small.[143] In the second study, HP ^{129}Xe NMR was used to distinguish the dynamic changes in Xe signals inside and outside the pores during the methanol adsorption and desorption processes, quantitatively providing the adsorption rates of methanol in both pores. The adsorption rate of methanol on the CNTs was 8−50 times faster than that on MCM-41.[144]

6. SUMMARY

Professor Bao has been a leading figure in heterogeneous catalysis and surface science for over 40 years. He has made remarkable academic contributions in establishment of "nano-confined catalysis" concepts, development of photoemission electron microscope (PEEM) and solid-state NMR techniques, and proposed the oxide−zeolite (OXZEO) catalysis process and the direct nonoxidative conversion of methane to olefins, aromatics, and hydrogen (MTOAH) as novel technologies for C1 molecular conversion. He has also mentored many young talents in catalysis, with numerous former students and postdoctoral researchers now recognized as key contributors to the international catalytic community. Although Professor Bao and his team are not known for high-volume productivity, their work is distinguished by unique insights and a strong personal imprint. Professor Bao is dedicated to addressing critical challenges in fossil resource utilization and renewable energy processes, pursuing demand-driven and problem-oriented research. As he once noted, "If the direction is right, the length of the journey is unimportant; by persevering, even an overlooked topic can regain attention". Professor Bao has exemplified this philosophy, leading his team for over 20 years in methane and syngas conversion, culminating in significant advancements in the field.

■ AUTHOR INFORMATION

Corresponding Authors

Qiang Fu − *State Key Laboratory of Catalysis, Dalian Institute of Chemical Physics, Chinese Academy of Sciences, Dalian 116023, China;* orcid.org/0000-0001-5316-6758;
Email: qfu@dicp.ac.cn
Ding Ma − *Beijing National Laboratory for Molecular Sciences, New Cornerstone Science Laboratory, College of Chemistry and Molecular Engineering, Peking University, Beijing 100871,*

China; orcid.org/0000-0002-3341-2998;
Email: dingma@pku.edu.cn

Authors

Feng Jiao − *State Key Laboratory of Catalysis, Dalian Institute of Chemical Physics, Chinese Academy of Sciences, Dalian 116023, China;* orcid.org/0000-0001-9376-7208

Rentao Mu − *State Key Laboratory of Catalysis, Dalian Institute of Chemical Physics, Chinese Academy of Sciences, Dalian 116023, China*

Shutao Xu − *State Key Laboratory of Catalysis, Dalian Institute of Chemical Physics, Chinese Academy of Sciences, Dalian 116023, China;* orcid.org/0000-0003-4722-8371

Hongyang Liu − *Shenyang National Laboratory for Materials Science, Institute of Metal Research, Chinese Academy of Sciences, Shenyang 110016, China; School of Materials Science and Engineering, University of Science and Technology of China, Hefei 230026, China;* orcid.org/0000-0003-2977-2867

Liang Yu − *State Key Laboratory of Catalysis, Dalian Institute of Chemical Physics, Chinese Academy of Sciences, Dalian 116023, China*

Dunfeng Gao − *State Key Laboratory of Catalysis, Dalian Institute of Chemical Physics, Chinese Academy of Sciences, Dalian 116023, China;* orcid.org/0000-0002-2472-7349

Yuefeng Song − *State Key Laboratory of Catalysis, Dalian Institute of Chemical Physics, Chinese Academy of Sciences, Dalian 116023, China*

Dehui Deng − *State Key Laboratory of Catalysis, Dalian Institute of Chemical Physics, Chinese Academy of Sciences, Dalian 116023, China;* orcid.org/0000-0001-9702-0531

Guoxiong Wang − *State Key Laboratory of Catalysis, Dalian Institute of Chemical Physics, Chinese Academy of Sciences, Dalian 116023, China; Department of Chemistry, Fudan University, Shanghai 200438, China;* orcid.org/0000-0001-6042-1171

Heng Zheng − *Southwest Institute of Chemical Co., Ltd., Chengdu 610225, China*

Weixin Huang − *Department of Chemical Physics, University of Science and Technology of China, Hefei 230026, China;* orcid.org/0000-0002-5025-3124

Xiulian Pan − *State Key Laboratory of Catalysis, Dalian Institute of Chemical Physics, Chinese Academy of Sciences, Dalian 116023, China;* orcid.org/0000-0002-5906-6675

Complete contact information is available at:
https://pubs.acs.org/10.1021/acscatal.4c06765

Notes

The authors declare no competing financial interest.

ACKNOWLEDGMENTS

The authors thank all colleagues and collaborators who contributed to the work presented in this article. The current team members and former co-workers of Xinhe Bao are listed at http://www.fruit.dicp.ac.cn/Member.htm.

REFERENCES

(1) Pan, X.; Fan, Z.; Chen, W.; Ding, Y.; Luo, H.; Bao, X. Enhanced ethanol production inside carbon-nanotube reactors containing catalytic particles. *Nat. Mater.* **2007**, *6* (7), 507−11.

(2) Chen, W.; Fan, Z.; Pan, X.; Bao, X. Effect of confinement in carbon nanotubes on the activity of Fischer−Tropsch iron catalyst. *J. Am. Chem. Soc.* **2008**, *130* (29), 9414−9.

(3) Pan, X.; Bao, X. Reactions over catalysts confined in carbon nanotubes. *Chem. Commun.* **2008**, No. 47, 6271−81.

(4) Fu, Q.; Li, W. X.; Yao, Y.; Liu, H.; Su, H. Y.; Ma, D.; Gu, X. K.; Chen, L.; Wang, Z.; Zhang, H.; Wang, B.; Bao, X. Interface-confined ferrous centers for catalytic oxidation. *Science* **2010**, *328* (5982), 1141−4.

(5) Pan, X.; Bao, X. The effects of confinement inside carbon nanotubes on catalysis. *Acc. Chem. Res.* **2011**, *44* (8), 553−62.

(6) Fu, Q.; Yang, F.; Bao, X. Interface-confined oxide nanostructures for catalytic oxidation reactions. *Acc. Chem. Res.* **2013**, *46* (8), 1692−701.

(7) Yang, F.; Deng, D. H.; Pan, X. L.; Fu, Q.; Bao, X. H. Understanding nano effects in catalysis. *Natl. Sci. Rev.* **2015**, *2* (2), 183−201.

(8) Chen, W.; Pan, X. L.; Bao, X. H. Tuning of redox properties of iron and iron oxides via encapsulation within carbon nanotubes. *J. Am. Chem. Soc.* **2007**, *129* (23), 7421−7426.

(9) Xiao, J. P.; Pan, X. L.; Guo, S. J.; Ren, P. J.; Bao, X. H. Toward fundamentals of confined catalysis in carbon nanotubes. *J. Am. Chem. Soc.* **2015**, *137* (1), 477−82.

(10) Guan, J.; Pan, X.; Liu, X.; Bao, X. Syngas segregation induced by confinement in carbon nanotubes: A combined first-principles and monte carlo study. *J. Phys. Chem. C* **2009**, *113* (52), 21687−21692.

(11) Fan, Z.; Chen, W.; Pan, X.; Bao, X. Catalytic conversion of syngas into C2 oxygenates over Rh-based catalysts—Effect of carbon supports. *Catal. Today* **2009**, *147* (2), 86−93.

(12) Yang, Z. Q.; Guo, S. J.; Pan, X. L.; Wang, J. H.; Bao, X. H. FeN nanoparticles confined in carbon nanotubes for CO hydrogenation. *Energy Environ. Sci.* **2011**, *4* (11), 4500−4503.

(13) Chen, X. Q.; Deng, D. H.; Pan, X. L.; Bao, X. H. Iron catalyst encapsulated in carbon nanotubes for CO hydrogenation to light olefins. *Chin. J. Catal.* **2015**, *36* (9), 1631−1637.

(14) Guo, S.; Pan, X.; Gao, H.; Yang, Z.; Zhao, J.; Bao, X. Probing the electronic effect of carbon nanotubes in catalysis: NH(3) synthesis with Ru nanoparticles. *Chem.—Eur. J.* **2010**, *16* (18), 5379−84.

(15) Gao, W. J.; Guo, S. J.; Zhang, H. B.; Pan, X. W.; Bao, X. H. Enhanced ammonia synthesis activity of Ru supported on nitrogen-doped carbon nanotubes. *Chin. J. Catal.* **2013**, *32* (8), 1418−1423.

(16) Deng, D. H.; Yu, L.; Chen, X. Q.; Wang, G. X.; Jin, L.; Pan, X. L.; Deng, J.; Sun, G. Q.; Bao, X. H. Iron encapsulated within pod-like carbon nanotubes for oxygen reduction reaction. *Angew. Chem., Int. Ed.* **2013**, *52* (1), 371−375.

(17) Deng, J.; Ren, P. J.; Deng, D. H.; Yu, L.; Yang, F.; Bao, X. H. Highly active and durable non-precious-metal catalysts encapsulated in carbon nanotubes for hydrogen evolution reaction. *Energy Environ. Sci.* **2014**, *7* (6), 1919−1923.

(18) Zhang, H. B.; Pan, X. L.; Han, X. W.; Liu, X. M.; Wang, X. F.; Shen, W. L.; Bao, X. H. Enhancing chemical reactions in a confined hydrophobic environment: an NMR study of benzene hydroxylation in carbon nanotubes. *Chem. Sci.* **2013**, *4* (3), 1075−1078.

(19) Zhang, F.; Jiao, F.; Pan, X. L.; Gao, K.; Xiao, J. P.; Zhang, S.; Bao, X. H. Tailoring the oxidation activity of Pt nanoclusters via encapsulation. *ACS Catal.* **2015**, *5* (2), 1381−1385.

(20) Mu, R. T.; Fu, Q.; Jin, L.; Yu, L.; Fang, G. Z.; Tan, D. L.; Bao, X. H. Visualizing chemical reactions confined under graphene. *Angew. Chem., Int. Ed.* **2012**, *51* (20), 4856−4859.

(21) Yao, Y. X.; Fu, Q.; Zhang, Y. Y.; Weng, X. F.; Li, H.; Chen, M. S.; Jin, L.; Dong, A. Y.; Mu, R. T.; Jiang, P.; Liu, L.; Bluhm, H.; Liu, Z.; Zhang, S. B.; Bao, X. H. Graphene cover-promoted metal-catalyzed reactions. *P. Natl. Acad. Sci. USA* **2014**, *111* (48), 17023−17028.

(22) Li, H. B.; Xiao, J. P.; Fu, Q.; Bao, X. H. Confined catalysis under two-dimensional materials. *P. Natl. Acad. Sci. USA* **2017**, *114* (23), 5930−5934.

(23) Fu, Q.; Bao, X. H. Surface chemistry and catalysis confined under two-dimensional materials. *Chem. Soc. Rev.* **2017**, *46* (7), 1842−1874.

(24) Ning, Y.; Wei, M.; Yu, L.; Yang, F.; Chang, R.; Liu, Z.; Fu, Q.; Bao, X. Nature of Interface Confinement Effect in Oxide/Metal Catalysts. *J. Phys. Chem. C* **2015**, *119* (49), 27556−27561.

(25) Guo, X. G.; Fu, Q.; Ning, Y. X.; Wei, M. M.; Li, M. R.; Zhang, S.; Jiang, Z.; Bao, X. H. Ferrous centers confined on core-shell

nanostructures for low-temperature CO oxidation. *J. Am. Chem. Soc.* **2012**, *134* (30), 12350−12353.

(26) Mu, R. T.; Fu, Q. A.; Xu, H.; Zhang, H. I.; Huang, Y. Y.; Jiang, Z.; Zhang, S. O.; Tan, D. L.; Bao, X. H. Synergetic effect of surface and subsurface Ni species at Pt-Ni bimetallic catalysts for CO oxidation. *J. Am. Chem. Soc.* **2011**, *133* (6), 1978−1986.

(27) Wang, D. Q.; Lin, L.; Zhang, R. K.; Mu, R. T.; Fu, Q. Stabilizing oxide nanolayer via interface confinement and surface hydroxylation. *J. Phys. Chem. Lett.* **2022**, *13* (28), 6566−6570.

(28) Li, R. T.; Mu, R. T.; Li, K.; Fan, Y. M.; Liu, C. H.; Ning, Y. X.; Li, M. R.; Fu, Q.; Bao, X. H. Dynamically Confined Active Silver Nanoclusters with Ultrawide Operating Temperature Window in CO oxidation. *Angew. Chem., Int. Ed.* **2025**, *64* (4), No. e202416852.

(29) Cui, X.; Li, H.; Wang, Y.; Hu, Y.; Hua, L.; Li, H.; Han, X.; Liu, Q.; Yang, F.; He, L.; Chen, X.; Li, Q.; Xiao, J.; Deng, D.; Bao, X. Room-Temperature Methane Conversion by Graphene-Confined Single Iron Atoms. *Chem.* **2018**, *4* (8), 1902−1910.

(30) Wang, L. S.; Tao, L. X.; Xie, M. S.; Xu, G. F.; Huang, J. S.; Xu, Y. D. Dehydrogenation and Aromatization of Methane under Nonoxidizing Conditions. *Catal. Lett.* **1993**, *21* (1−2), 35−41.

(31) Ma, S. Q.; Guo, X. G.; Zhao, L. X.; Scott, S.; Bao, X. H. Recent progress in methane dehydroaromatization: From laboratory curiosities to promising technology. *J. Energy Chem.* **2013**, *22* (1), 1−20.

(32) Schwach, P.; Pan, X. L.; Bao, X. H. Direct conversion of methane to value-added chemicals over heterogeneous catalysts: challenges and prospects. *Chem. Rev.* **2017**, *117* (13), 8497−8520.

(33) Shu, Y. Y.; Ma, D.; Xu, L. Y.; Xu, Y. D.; Bao, X. H. Methane dehydro-aromatization over Mo/MCM-22 catalysts: a highly selective catalyst for the formation of benzene. *Catal. Lett.* **2000**, *70* (1−2), 67−73.

(34) Ma, D.; Shu, Y. Y.; Cheng, M. J.; Xu, Y. D.; Bao, X. H. On the induction period of methane aromatization over Mo-based catalysts. *J. Catal.* **2000**, *194* (1), 105−114.

(35) Ma, D.; Wang, D. Z.; Su, L. L.; Shu, Y. Y.; Xu, Y.; Bao, X. H. Carbonaceous deposition on Mo/HMCM-22 catalysts for methane aromatization: A TP technique investigation. *J. Catal.* **2002**, *208* (2), 260−269.

(36) Ma, D.; Lu, Y.; Su, L. L.; Xu, Z. S.; Tian, Z. J.; Xu, Y.; Lin, L. W.; Bao, X. H. Remarkable improvement on the methane aromatization reaction: A highly selective and coking-resistant catalyst. *J. Phys. Chem. B* **2002**, *106* (34), 8524−8530.

(37) Ma, D.; Shu, Y.; Han, X.; Liu, X.; Xu, Y.; Bao, X. Mo/HMCM-22 Catalysts for Methane Dehydroaromatization: A Multinuclear MAS NMR Study. *J. Phys. Chem. B* **2001**, *105* (9), 1786−1793.

(38) Cheng, M. J.; Tan, D. L.; Liu, X. M.; Han, X. W.; Bao, X. H.; Lin, L. W. Effect of aluminum on the formation of zeolite MCM-22 and kenyaite. *Micropor. Mesopor. Mater.* **2001**, *42* (2−3), 307−316.

(39) Chen, F.; Deng, F.; Cheng, M.; Yue, Y.; Ye, C.; Bao, X. Preferential occupation of xenon in zeolite MCM-22 as revealed by 129Xe NMR spectroscopy. *J. Phys. Chem. B* **2001**, *105* (39), 9426−9432.

(40) Ma, D.; Deng, F.; Fu, R. Q.; Dan, X. W.; Bao, X. H. MAS MMR studies on the dealumination of zeolite MCM-22. *J. Phys. Chem. B* **2001**, *105* (9), 1770−1779.

(41) Sun, C. Y.; Fang, G. Z.; Guo, X. G.; Hu, Y. L.; Ma, S. Q.; Yang, T. H.; Han, J.; Ma, H.; Tan, D. L.; Bao, X. H. Methane dehydroaromatization with periodic CH4-H2 switch: A promising process for aromatics and hydrogen. *J. Energy Chem.* **2015**, *24* (3), 257−263.

(42) Guo, X. G.; Fang, G. Z.; Li, G.; Ma, H.; Fan, H. J.; Yu, L.; Ma, C.; Wu, X.; Deng, D. H.; Wei, M. M.; Tan, D. L.; Si, R.; Zhang, S.; Li, J. Q.; Sun, L. T.; Tang, Z. C.; Pan, X. L.; Bao, X. H. Direct, nonoxidative conversion of methane to ethylene, aromatics, and hydrogen. *Science* **2014**, *344* (6184), 616−619.

(43) Han, S. J.; Lee, S. W.; Kim, H. W.; Kim, S. K.; Kim, Y. T. Nonoxidative direct conversion of methane on silica-based iron catalysts: effect of catalytic surface. *ACS Catal.* **2019**, *9* (9), 7984−7997.

(44) Hao, J. Q.; Schwach, P.; Li, L. L.; Guo, X. G.; Weng, J. B.; Zhang, H. L.; Shen, H.; Fang, G. Z.; Huang, X.; Pan, X. L.; Xiao, C. L.; Yang, X. M.; Bao, X. H. Direct experimental detection of hydrogen radicals in non-oxidative methane catalytic reaction. *J. Energy Chem.* **2021**, *52*, 372−376.

(45) Bae, J.; Hashemi, J.; Yun, D.; Kim, D.; Choo, D. H.; Goldsmith, C. F.; Peterson, A. A. Non-oxidative methane conversion by Fe single site catalysts: quantifying temperature limitations imposed by gas-phase pyrolysis. *Catal. Sci. Technol.* **2022**, *12* (22), 6903−6919.

(46) Eggart, D.; Huang, X.; Zimina, A.; Yang, J. Z.; Pan, Y.; Pan, X. L.; Grunwaldt, J. D. Operando XAS study of Pt-doped CeO2 for the nonoxidative conversion of methane. *ACS Catal.* **2022**, *12* (7), 3897−3908.

(47) Sim, E. H.; Lee, S. W.; Lee, J. J.; Han, S. J.; Shin, J. H.; Lee, G.; Ko, S.; Lee, K. Y.; Kim, Y. T. Effect of silicon carbide-based iron catalyst on reactor optimization for non-oxidative direct conversion of methane. *J. Energy Chem.* **2023**, *81*, 519−532.

(48) Han, S. J.; Gebreyohannes, T. G.; Woo lee, S.; Kim, S. K.; Kim, H. W.; Shin, J. H.; Kim, Y. T. Methane direct conversion to olefins, aromatics, and hydrogen over silica entrapped bimetallic MeFe-SiO2 (Me = Co, Ni, Pd, Pt) catalysts. *Mol. Catal.* **2023**, *535*, No. 112864.

(49) Lee, J. J.; Lee, S.; Bae, Y. S.; Lee, J.; Kim, Y. T. Non-oxidative direct conversion of methane: Improved reactivity via linkage with dehydroaromatization. *Fuel Process. Technol.* **2024**, *256*, No. 108067.

(50) Lee, S. W.; Gebreyohannes, T. G.; Shin, J. H.; Kim, H. W.; Kim, Y. T. Carbon-efficient reaction optimization of nonoxidative direct methane conversion based on the integrated reactor system. *Chem. Eng. J.* **2024**, *481*, No. 148286.

(51) Huang, X.; Eggart, D.; Qin, G.; Sarma, B. B.; Gaur, A.; Yang, J.; Pan, Y.; Li, M.; Hao, J.; Yu, H.; Zimina, A.; Guo, X.; Xiao, J.; Grunwaldt, J. D.; Pan, X.; Bao, X. Methyl radical chemistry in non-oxidative methane activation over metal single sites. *Nat. Commun.* **2023**, *14* (1), 5716.

(52) An, Z. J.; Pan, X. L.; Liu, X. M.; Han, X. W.; Bao, X. H. Combined redox couples for catalytic oxidation of methane by dioxygen at low temperatures. *J. Am. Chem. Soc.* **2006**, *128* (50), 16028−16029.

(53) Torres Galvis, H. M.; de Jong, K. P. Catalysts for Production of Lower Olefins from Synthesis Gas: A Review. *ACS Catal.* **2013**, *3* (9), 2130−2149.

(54) Jiao, F.; Li, J.; Pan, X.; Xiao, J.; Li, H.; Ma, H.; Wei, M.; Pan, Y.; Zhou, Z.; Li, M.; Miao, S.; Li, J.; Zhu, Y.; Xiao, D.; He, T.; Yang, J.; Qi, F.; Fu, Q.; Bao, X. Selective conversion of syngas to light olefins. *Science* **2016**, *351* (6277), 1065−8.

(55) Zhu, Y. F.; Pan, X. L.; Jiao, F.; Li, J.; Yang, J. H.; Ding, M. Z.; Han, Y.; Liu, Z.; Bao, X. H. Role of manganese oxide in syngas conversion to light olefins. *ACS Catal.* **2017**, *7* (4), 2800−2804.

(56) Yang, J.; Pan, X.; Jiao, F.; Li, J.; Bao, X. Direct conversion of syngas to aromatics. *Chem. Commun.* **2017**, *53* (81), 11146−11149.

(57) Jiao, F.; Pan, X.; Gong, K.; Chen, Y.; Li, G.; Bao, X. Shape-selective zeolites promote ethylene formation from syngas via a ketene intermediate. *Angew. Chem., Int. Ed.* **2018**, *57* (17), 4692−4696.

(58) Li, N.; Jiao, F.; Pan, X. L.; Ding, Y.; Feng, J. Y.; Bao, X. H. Size effects of ZnO nanoparticles in bifunctional catalysts for selective syngas conversion. *ACS Catal.* **2019**, *9* (2), 960−966.

(59) Li, N.; Jiao, F.; Pan, X.; Chen, Y.; Feng, J.; Li, G.; Bao, X. High-quality gasoline directly from syngas by dual metal oxide-zeolite (OX-ZEO) catalysis. *Angew. Chem., Int. Ed.* **2019**, *58* (22), 7400−7404.

(60) Li, G.; Jiao, F.; Miao, D. Y.; Wang, Y.; Pan, X. L.; Yokoi, T.; Meng, X. J.; Xiao, F. S.; Parvulescu, A. N.; Müller, U.; Bao, X. H. Selective conversion of syngas to propane over ZnCrO -SSZ-39 OX-ZEO catalysts. *J. Energy Chem.* **2019**, *36*, 141−147.

(61) Yang, J. H.; Gong, K.; Miao, D. Y.; Jiao, F.; Pan, X. L.; Meng, X. J.; Xiao, F. S.; Bao, X. H. Enhanced aromatic selectivity by the sheet-like ZSM-5 in syngas conversion. *J. Energy Chem.* **2019**, *35*, 44−48.

(62) Li, G.; Jiao, F.; Pan, X. L.; Li, N.; Miao, D. Y.; Li, L.; Bao, X. H. Role of SAPO-18 acidity in direct syngas conversion to light olefins. *ACS Catal.* **2020**, *10* (21), 12370−12375.

(63) Chen, Y.; Gong, K.; Jiao, F.; Pan, X.; Hou, G.; Si, R.; Bao, X. C-C bond formation in syngas conversion over zinc sites grafted on ZSM-5 zeolite. *Angew. Chem., Int. Ed.* **2020**, *59* (16), 6529−6534.

(64) Ding, Y.; Jiao, F.; Pan, X. L.; Ji, Y.; Li, M. R.; Si, R.; Pan, Y.; Hou, G. J.; Bao, X. H. Effects of Proximity-Dependent Metal Migration on

Bifunctional Composites Catalyzed Syngas to Olefins. *ACS Catal.* **2021**, *11* (15), 9729−9737.

(65) Li, N.; Zhu, Y.; Jiao, F.; Pan, X.; Jiang, Q.; Cai, J.; Li, Y.; Tong, W.; Xu, C.; Qu, S.; Bai, B.; Miao, D.; Liu, Z.; Bao, X. Steering the reaction pathway of syngas-to-light olefins with coordination unsaturated sites of ZnGaOx spinel. *Nat. Commun.* **2022**, *13* (1), 2742.

(66) Jiao, F.; Bai, B.; Li, G.; Pan, X.; Ye, Y.; Qu, S.; Xu, C.; Xiao, J.; Jia, Z.; Liu, W.; Peng, T.; Ding, Y.; Liu, C.; Li, J.; Bao, X. Disentangling the activity-selectivity trade-off in catalytic conversion of syngas to light olefins. *Science* **2023**, *380* (6646), 727−730.

(67) Chen, Y.; Han, S.; Pan, X.; Jiao, F.; Liu, W.; Pan, Y.; Bao, X. Visualization of the Active Sites of Zinc-Chromium Oxides and the CO/H2 Activation Mechanism in Direct Syngas Conversion. *J. Am. Chem. Soc.* **2024**, *146* (3), 1887−1893.

(68) Zhang, Y.; Gao, P.; Jiao, F.; Chen, Y.; Ding, Y.; Hou, G.; Pan, X.; Bao, X. Chemistry of ketene transformation to gasoline catalyzed by H-SAPO-11. *J. Am. Chem. Soc.* **2022**, *144* (40), 18251−18258.

(69) Feng, J. Y.; Miao, D. Y.; Ding, Y. L.; Jiao, F.; Pan, X. L.; Bao, X. H. Direct synthesis of isoparaffin-rich gasoline from syngas. *ACS Energy Lett.* **2022**, *7* (4), 1462−1468.

(70) Chen, Y. X.; Jiao, F.; Pan, X. L.; Bao, X. H. Role of Sn/ZSM-5 in direct syngas conversion. *Catal. Sci. Technol.* **2022**, *12* (18), 5533−5539.

(71) Wang, H.; Jiao, F.; Ding, Y.; Liu, W.; Xu, Z.; Pan, X.; Bao, X. Dynamic confinement of SAPO-17 cages on the selectivity control of syngas conversion. *Natl. Sci. Rev.* **2022**, *9* (9), No. nwac146.

(72) Pan, X.; Jiao, F.; Miao, D.; Bao, X. Oxide-zeolite-based composite catalyst concept that enables syngas chemistry beyond fischer-tropsch synthesis. *Chem. Rev.* **2021**, *121* (11), 6588−6609.

(73) Bai, B.; Guo, C.; Jiao, F.; Xiao, J.; Ding, Y.; Qu, S.; Pan, Y.; Pan, X.; Bao, X. Tuning the crystal phase to form MnGaOx-spinel for highly efficient syngas to light olefins. *Angew. Chem., Int. Ed.* **2023**, *62* (25), No. e202217701.

(74) Ding, Y. L.; Zhao, Y. Z.; Miao, D. Y.; Wang, Z. L.; Feng, J. Y.; Jiao, F.; Pan, X. L.; Bao, X. H. Al distribution of MWW zeolites and its correlation with catalytic performance in direct syngas conversion. *J. Phys. Chem. C* **2024**, *128* (11), 4508−4515.

(75) Feng, J. Y.; Miao, D. Y.; Ding, Y. L.; Jiao, F.; Pan, X. L.; Bao, X. H. Stability of ZnMOx−SAPO-11 (OXZEO) composite catalysts for syngas conversion to gasoline. *Catal. Sci. Technol.* **2024**, *14* (5), 1209−1215.

(76) Wu, H. H.; Li, H. B.; Zhao, X. F.; Liu, Q. F.; Wang, J.; Xiao, J. P.; Xie, S. H.; Si, R.; Yang, F.; Miao, S.; Guo, X. G.; Wang, G. X.; Bao, X. H. Highly doped and exposed Cui−N active sites within graphene towards efficient oxygen reduction for zinc−air batteries. *Energy Environ. Sci.* **2016**, *9* (12), 3736−3745.

(77) Wang, J.; Gao, D. F.; Wang, G. X.; Miao, S.; Wu, H. H.; Li, J. Y.; Bao, X. H. Cobalt nanoparticles encapsulated in nitrogen-doped carbon as a bifunctional catalyst for water electrolysis. *J. Mater. Chem. A* **2014**, *2* (47), 20067−20074.

(78) Gao, D.; Zhou, H.; Wang, J.; Miao, S.; Yang, F.; Wang, G.; Wang, J.; Bao, X. Size-dependent electrocatalytic reduction of CO2 over Pd nanoparticles. *J. Am. Chem. Soc.* **2015**, *137* (13), 4288−91.

(79) Gao, D. F.; Zhou, H.; Cai, F.; Wang, D. N.; Hu, Y. F.; Jiang, B.; Cai, W. B.; Chen, X. Q.; Si, R.; Yang, F.; Miao, S.; Wang, J. G.; Wang, G. X.; Bao, X. H. Switchable CO2 electroreduction via engineering active phases of Pd nanoparticles. *Nano Res.* **2017**, *10* (6), 2181−2191.

(80) Gao, D.; Zhang, Y.; Zhou, Z.; Cai, F.; Zhao, X.; Huang, W.; Li, Y.; Zhu, J.; Liu, P.; Yang, F.; Wang, G.; Bao, X. Enhancing CO2 electroreduction with the metal-oxide interface. *J. Am. Chem. Soc.* **2017**, *139* (16), 5652−5655.

(81) Cai, F.; Gao, D.; Zhou, H.; Wang, G.; He, T.; Gong, H.; Miao, S.; Yang, F.; Wang, J.; Bao, X. Electrochemical promotion of catalysis over Pd nanoparticles for CO(2) reduction. *Chem. Sci.* **2017**, *8* (4), 2569−2573.

(82) Yan, C. C.; Li, H. B.; Ye, Y. F.; Wu, H. H.; Cai, F.; Si, R.; Xiao, J. P.; Miao, S.; Xie, S. H.; Yang, F.; Li, Y. S.; Wang, G. X.; Bao, X. H. Coordinatively unsaturated nickel−nitrogen sites towards selective and high-rate CO2electroreduction. *Energy Environ. Sci.* **2018**, *11* (5), 1204−1210.

(83) Lin, L.; Liu, T.; Xiao, J.; Li, H.; Wei, P.; Gao, D.; Nan, B.; Si, R.; Wang, G.; Bao, X. Enhancing CO2 electroreduction to methane with a cobalt phthalocyanine and zinc-nitrogen-carbon tandem catalyst. *Angew. Chem., Int. Ed.* **2020**, *59* (50), 22408−22413.

(84) Gao, D. F.; Wei, P. F.; Li, H. F.; Lin, L.; Wang, G. X.; Bao, X. H. Designing electrolyzers for electrocatalytic CO2 reduction. *Acta Phys-Chim Sin* **2020**, *0* (0), 2009021−0.

(85) Li, H.; Liu, T.; Wei, P.; Lin, L.; Gao, D.; Wang, G.; Bao, X. High-rate CO2 electroreduction to C2+ products over a copper-copper iodide catalyst. *Angew. Chem., Int. Ed.* **2021**, *60* (26), 14329−14333.

(86) Wei, P.; Gao, D.; Liu, T.; Li, H.; Sang, J.; Wang, C.; Cai, R.; Wang, G.; Bao, X. Coverage-driven selectivity switch from ethylene to acetate in high-rate CO2/CO electrolysis. *Nat. Nanotechnol.* **2023**, *18* (3), 299−306.

(87) Li, H. F.; Li, H. B.; Wei, P. F.; Wang, Y.; Zang, Y. P.; Gao, D. F.; Wang, G. X.; Bao, X. H. Tailoring acidic microenvironments for carbon-efficient CO2 electrolysis over a Ni−N−C catalyst in a membrane electrode assembly electrolyzer. *Energy Environ. Sci.* **2023**, *16* (4), 1502−1510.

(88) Li, H. F.; Wei, P. F.; Liu, T. F.; Li, M. R.; Wang, C.; Li, R. T.; Ye, J. Y.; Zhou, Z. Y.; Sun, S. G.; Fu, Q.; Gao, D. F.; Wang, G. X.; Bao, X. H. CO electrolysis to multicarbon products over grain boundary-rich Cu nanoparticles in membrane electrode assembly electrolyzers. *Nat. Commun.* **2024**, *15* (1), 4603.

(89) Song, Y.; Zhang, X.; Xie, K.; Wang, G.; Bao, X. High-temperature CO2 electrolysis in solid oxide electrolysis cells: developments, challenges, and prospects. *Adv. Mater.* **2019**, *31* (50), No. e1902033.

(90) Feng, W. C.; Liu, T. F.; Li, R. T.; Li, J. W.; Zhang, X. M.; Liu, Q. X.; Wang, J. H.; Li, M. R.; Fu, Q.; Song, Y. F.; Wang, G. X.; Bao, X. H. Optimizing the electronic structures of CaSr1-Co0.7Fe0.3O3-δ anodes for high-temperature oxygen evolution reaction. *Chem. Catal.* **2023**, *3* (3), No. 100504.

(91) Liu, Q.; Shen, F.; Song, G.; Liu, T.; Feng, W.; Li, R.; Zhang, X.; Li, M.; He, L.; Zheng, X.; Yin, S.; Yin, G.; Song, Y.; Wang, G.; Bao, X. Tailoring ion ordering in perovskite oxide for high-temperature oxygen evolution reaction. *Angew. Chem., Int. Ed.* **2023**, *62* (32), No. e202307057.

(92) Song, Y.; Zhou, S.; Dong, Q.; Li, Y.; Zhang, X.; Ta, N.; Liu, Z.; Zhao, J.; Yang, F.; Wang, G.; Bao, X. Oxygen evolution reaction over the Au/YSZ interface at high temperature. *Angew. Chem., Int. Ed.* **2019**, *58* (14), 4617−4621.

(93) Song, Y.; Lin, L.; Feng, W.; Zhang, X.; Dong, Q.; Li, X.; Lv, H.; Liu, Q.; Yang, F.; Liu, Z.; Wang, G.; Bao, X. Interfacial enhancement by gamma-Al2O3 of electrochemical oxidative dehydrogenation of ethane to ethylene in solid oxide electrolysis cells. *Angew. Chem., Int. Ed.* **2019**, *58* (45), 16043−16046.

(94) Guo, Y. G.; Wang, S.; Li, R. T.; Yu, J. C.; Zhang, X. M.; Li, M. R.; Zheng, X. S.; Zhu, J. F.; Song, Y. F.; Wang, G. X. In situ exsolved CoFe alloy nanoparticles for stable anodic methane reforming in solid oxide electrolysis cells. *Joule* **2024**, *8* (7), 2016−2032.

(95) Lv, H.; Liu, T.; Zhang, X.; Song, Y.; Matsumoto, H.; Ta, N.; Zeng, C.; Wang, G.; Bao, X. Atomic-scale insight into exsolution of CoFe alloy nanoparticles in La0. 4Sr0. 6Co0. 2Fe0. 7Mo0. 1O3− δ with efficient CO2 electrolysis. *Angew. Chem., Int. Ed.* **2020**, *59* (37), 15968−15973.

(96) Lv, H.; Lin, L.; Zhang, X.; Song, Y.; Matsumoto, H.; Zeng, C.; Ta, N.; Liu, W.; Gao, D.; Wang, G. In Situ investigation of reversible exsolution/dissolution of CoFe alloy nanoparticles in a Co-doped Sr2Fe1. 5Mo0. 5O6− δ cathode for CO2 electrolysis. *Adv. Mater.* **2020**, *32* (6), No. 1906193.

(97) Lv, H.; Lin, L.; Zhang, X.; Li, R.; Song, Y.; Matsumoto, H.; Ta, N.; Zeng, C.; Fu, Q.; Wang, G.; Bao, X. Promoting exsolution of RuFe alloy nanoparticles on Sr2Fe1.4Ru0.1Mo0.5O6-delta via repeated redox manipulations for CO2 electrolysis. *Nat. Commun.* **2021**, *12* (1), 5665.

(98) Song, Y.; Min, J.; Guo, Y.; Li, R.; Zou, G.; Li, M.; Zang, Y.; Feng, W.; Yao, X.; Liu, T.; Zhang, X.; Yu, J.; Liu, Q.; Zhang, P.; Yu, R.; Cao,

X.; Zhu, J.; Dong, K.; Wang, G.; Bao, X. Surface activation by single Ru atoms for enhanced high-temperature CO2 electrolysis. *Angew. Chem., Int. Ed.* **2024**, *63* (5), No. e202313361.

(99) Fu, Y.; Wang, S.; Wang, Y.; Wei, P.; Shao, J.; Liu, T.; Wang, G.; Bao, X. Enhancing electrochemical nitrate reduction to ammonia over Cu nanosheets via facet tandem catalysis. *Angew. Chem., Int. Ed.* **2023**, *62* (26), No. e202303327.

(100) Deng, J.; Ren, P. J.; Deng, D. H.; Bao, X. H. Enhanced electron penetration through an ultrathin graphene layer for highly efficient catalysis of the hydrogen evolution reaction. *Angew. Chem., Int. Ed.* **2015**, *54* (7), 2100−2104.

(101) Cui, X. J.; Ren, P. J.; Deng, D. H.; Deng, J.; Bao, X. H. Single layer graphene encapsulating non-precious metals as high-performance electrocatalysts for water oxidation. *Energy Environ. Sci.* **2016**, *9* (1), 123−129.

(102) Tu, Y. C.; Ren, P. J.; Deng, D. H.; Bao, X. H. Structural and electronic optimization of graphene encapsulating binary metal for highly efficient water oxidation. *Nano Energy* **2018**, *52*, 494−500.

(103) Yu, L.; Deng, D.; Bao, X. Chain mail for catalysts. *Angew. Chem., Int. Ed.* **2020**, *59* (36), 15294−15297.

(104) Deng, J.; Li, H. B.; Xiao, J. P.; Tu, Y. C.; Deng, D. H.; Yang, H. X.; Tian, H. F.; Li, J. Q.; Ren, P. J.; Bao, X. H. Triggering the electrocatalytic hydrogen evolution activity of the inert two-dimensional MoS surface single-atom metal doping. *Energy Environ. Sci.* **2015**, *8* (5), 1594−1601.

(105) Deng, D. H.; Chen, X. Q.; Yu, L.; Wu, X.; Liu, Q. F.; Liu, Y.; Yang, H. X.; Tian, H. F.; Hu, Y. F.; Du, P. P.; Si, R.; Wang, J. H.; Cui, X. J.; Li, H. B.; Xiao, J. P.; Xu, T.; Deng, J.; Yang, F.; Duchesne, P. N.; Zhang, P.; Zhou, J. G.; Sun, L. T.; Li, J. Q.; Pan, X. L.; Bao, X. H. A single iron site confined in a graphene matrix for the catalytic oxidation of benzene at room temperature. *Sci. Adv.* **2015**, *1* (11), No. e1500462.

(106) Zheng, Y.; Wang, J.; Yu, B.; Zhang, W.; Chen, J.; Qiao, J.; Zhang, J. A review of high temperature co-electrolysis of H2O and CO2 to produce sustainable fuels using solid oxide electrolysis cells (SOECs): advanced materials and technology. *Chem. Soc. Rev.* **2017**, *46* (5), 1427−1463.

(107) Wang, Z.; Huang, J.; Wang, L.; Liu, Y.; Liu, W.; Zhao, S.; Liu, Z. Q. Cation-tuning induced d-Band center modulation on Co-based spinel oxide for oxygen reduction/evolution reaction. *Angew. Chem., Int. Ed.* **2022**, *61* (16), No. e202114696.

(108) Feng, W.; Liu, T.; Li, R.; Li, J.; Zhang, X.; Liu, Q.; Wang, J.; Li, M.; Fu, Q.; Song, Y. Optimizing the electronic structures of CaxSr1-xCo0. 7Fe0. 3O3-δ anodes for high-temperature oxygen evolution reaction. *Chem. Catal.* **2023**, *3* (3), No. 100504.

(109) Pei, K.; Zhou, Y. C.; Ding, Y.; Xu, K.; Zhang, H.; Yuan, W.; Sasaki, K.; Choi, Y. M.; Liu, M. L.; Chen, Y. An improved oxygen reduction reaction activity and CO2-tolerance of La0.6Sr0.4Co0.2-Fe0.8O3-δ achieved by a surface modification with barium cobaltite coatings. *J. Power Sources* **2021**, *514*, No. 230573.

(110) Song, Y.; Zhou, S.; Dong, Q.; Li, Y.; Zhang, X.; Ta, N.; Liu, Z.; Zhao, J.; Yang, F.; Wang, G. Oxygen Evolution Reaction over the Au/YSZ Interface at High Temperature. *Angew. Chem., Int. Ed.* **2019**, *58* (14), 4617−4621.

(111) Wang, Y.; Liu, T. F.; Lei, L. B.; Chen, F. L. Methane assisted solid oxide co-electrolysis process for syngas production. *J. Power Sources* **2017**, *344*, 119−127.

(112) Lv, H.; Lin, L.; Zhang, X.; Li, R.; Song, Y.; Matsumoto, H.; Ta, N.; Zeng, C.; Fu, Q.; Wang, G. Promoting exsolution of RuFe alloy nanoparticles on Sr2Fe1. 4Ru0. 1Mo0. 5O6− δ via repeated redox manipulations for CO2 electrolysis. *Nat. Commun.* **2021**, *12* (1), 5665.

(113) Bao, X.; Barth, J. V.; Lehmpfuhl, G.; Schuster, R.; Uchida, Y.; Schlögl, R.; Ertl, G. Oxygen-induced restructuring of Ag(111). *Surf. Sci.* **1993**, *284* (1−2), 14−22.

(114) Schubert, H.; Tegtmeyer, U.; Herein, D.; Bao, X.; Muhler, M.; Schlögl, R. On the relation between catalytic performance and microstructure of polycrystalline silver in the partial oxidation of methanol. *Catal. Lett.* **1995**, *33* (3−4), 305−319.

(115) Bao, X.; Muhler, M.; Pettinger, B.; Schlögl, R.; Ertl, G. On the nature of the active state of silver during catalytic oxidation of methanol. *Catal. Lett.* **1993**, *22* (3), 215−225.

(116) Bao, X.; Muhler, M.; Schedel-Niedrig, T.; Schlogl, R. Interaction of oxygen with silver at high temperature and atmospheric pressure: A spectroscopic and structural analysis of a strongly bound surface species. *Phys. Rev. B* **1996**, *54* (3), 2249−2262.

(117) Bao, X. Catalytic characters of the nano-confined systems. *Sci. Chin. Chem.* **2009**, *39* (10), 1125−1133.

(118) Huang, W. X.; Zhai, R. S.; Bao, X. H. Direct observation of subsurface oxygen on the defects of Pd(100). *Surf. Sci.* **1999**, *439* (1−3), L803−L807.

(119) Huang, W. X.; Zhai, R. S.; Bao, X. H. Investigation of oxygen adsorption on Pd (100) with defects. *Appl. Surf. Sci.* **2000**, *158* (3−4), 287−291.

(120) Nepijko, S. A.; Sedov, N. N.; Schönhense, G.; Escher, M.; Bao, X. H.; Huang, W. X. Resolution deterioration in emission electron microscopy due to object roughness. *Ann. Phys-Berlin.* **2000**, *512* (6), 441−451.

(121) Huang, W. X.; Teng, J. W.; Bao, X. H. Studies on the surface migration of adsorbed oxygen from noble metals to silver over binary catalysts. *Surf. Inter. Anal.* **2001**, *32* (1), 179−182.

(122) Huang, W.; Bao, X. Adsorption and reaction of CO and O2 on the Ag/Pt(110) surface studied by photoemission electron microscopy. *Chin. Sci. Bull.* **2001**, *46* (12), 998−1001.

(123) Huang, W. X.; Bao, X. H.; Rotermund, H. H.; Ertl, G. CO adsorption on the O-saturated Ag/Pt(110) composite surface: Direct observation of the diffusion of adsorbed CO from strongly bound Pt sites to weakly bound Ag sites. *J. Phys. Chem. B* **2002**, *106* (22), 5645−5647.

(124) Cui, Y.; Fu, Q.; Zhang, H.; Tan, D. L.; Bao, X. H. Dynamic characterization of graphene growth and etching by oxygen on Ru(0001) by photoemission electron microscopy. *J. Phys. Chem. C* **2009**, *113* (47), 20365−20370.

(125) Yao, Y.; Fu, Q.; Tan, D.; Bao, X. A comparative study of CCl4 reactions on Ag and Si surfaces by in situ ultraviolet photoemission electron microscopy. *J. Phys-Condens. Mater.* **2009**, *21* (31), No. 314014.

(126) Cui, Y.; Fu, Q.; Bao, X. Dynamic observation of layer-by-layer growth and removal of graphene on Ru(0001). *Phys. Chem. Chem. Phys.* **2010**, *12* (19), 5053−7.

(127) Cui, Y.; Gao, J. F.; Jin, L.; Zhao, J. J.; Tan, D. L.; Fu, Q.; Bao, X. H. An exchange intercalation mechanism for the formation of a two-dimensional Si structure underneath graphene. *Nano Res.* **2012**, *5* (5), 352−360.

(128) Jin, L.; Fu, Q.; Yang, Y.; Bao, X. H. A comparative study of intercalation mechanism at graphene/Ru(0001) interface. *Surf. Sci.* **2013**, *617*, 81−86.

(129) Zhang, Y. H.; Wei, M. M.; Fu, Q.; Bao, X. H. Oxygen intercalation under hexagonal boron nitride (h-BN) on Pt(111). *Sci. Bull.* **2015**, *60* (18), 1572−1579.

(130) Yang, Y.; Fu, Q.; Wei, M. M.; Bluhm, H.; Bao, X. H. Stability of BN/metal interfaces in gaseous atmosphere. *Nano Res.* **2015**, *8* (1), 227−237.

(131) Ning, Y. X.; Fu, Q.; Bao, X. H. Applications of PEEM/LEEM in dynamic studies of surface physics and chemistry of two-dimensional atomic crystals. *Acta. Phys-Chim. Sin.* **2016**, *32* (1), 171−182.

(132) Lu, X.; Hao, Q.; Cen, M.; Zhang, G.; Sun, J.; Mao, L.; Cao, T.; Zhou, C.; Jiang, P.; Yang, X.; Bao, X. Observation and manipulation of visible edge plasmons in Bi2Te3 nanoplates. *Nano Lett.* **2018**, *18* (5), 2879−2884.

(133) Wei, W.; Lin, L.; Zhang, G. H.; Ye, X. Q.; Bin, R.; Meng, C. X.; Ning, Y. X.; Fu, Q.; Bao, X. H. Effect of near-surface dopants on the epitaxial growth of h-BN on metal surfaces. *Adv. Mater. Interfaces.* **2019**, *6* (10), No. 1801906.

(134) Ning, Y.; Fu, Q.; Li, Y.; Zhao, S.; Wang, C.; Breitschaft, M.; Hagen, S.; Schaff, O.; Bao, X. A near ambient pressure photoemission electron microscope (NAP-PEEM). *Ultramicroscopy* **2019**, *200*, 105−110.

(135) Ning, Y.; Li, Y.; Wang, C.; Li, R.; Zhang, F.; Zhang, S.; Wang, Z.; Yang, F.; Zong, N.; Peng, Q.; Xu, Z.; Wang, X.; Li, R.; Breitschaft, M.; Hagen, S.; Schaff, O.; Fu, Q.; Bao, X. Tunable deep ultraviolet laser based near ambient pressure photoemission electron microscope for surface imaging in the millibar regime. *Rev. Sci. Instrum.* **2020**, *91* (11), No. 113704.

(136) Zhang, W. P.; Xu, S. T.; Han, X. W.; Bao, X. H. In situ solid-state NMR for heterogeneous catalysis: a joint experimental and theoretical approach. *Chem. Soc. Rev.* **2012**, *41* (1), 192−210.

(137) Zhang, W.; Ma, D.; Liu, X.; Liu, X.; Bao, X. Perfluorotributylamine as a probe molecule for distinguishing internal and external acidic sites in zeolites by high-resolution 1H MAS NMR spectroscopy. *Chem. Commun.* **1999**, No. 12, 1091−1092.

(138) Xu, S.; Zhang, W.; Liu, X.; Han, X.; Bao, X. Enhanced in situ continuous-flow MAS NMR for reaction kinetics in the nanocages. *J. Am. Chem. Soc.* **2009**, *131* (38), 13722−13727.

(139) Ma, D.; Shu, Y.; Zhang, W.; Han, X.; Xu, Y.; Bao, X. In situ 1H MAS NMR spectroscopic observation of proton species on a Mo-modified HZSM-5 zeolite catalyst for the dehydroaromatization of methane. *Angew. Chem., Int. Ed.* **2000**, *39* (16), 2928−2931.

(140) Zhang, W.; Ma, D.; Han, X.; Liu, X.; Bao, X.; Guo, X.; Wang, X. Methane Dehydro-aromatization over Mo/HZSM-5 in the Absence of Oxygen: A Multinuclear Solid-State NMR Study of the Interaction between Supported Mo Species and HZSM-5 Zeolite with Different Crystal Sizes. *J. Catal.* **1999**, *188* (2), 393−402.

(141) Zheng, H.; Ma, D.; Bao, X.; Hu, J. Z.; Kwak, J. H.; Wang, Y.; Peden, C. H. Direct observation of the active center for methane dehydroaromatization using an ultrahigh field 95Mo NMR spectroscopy. *J. Am. Chem. Soc.* **2008**, *130* (12), 3722−3.

(142) Ma, D.; Han, X.; Zhou, D.; Yan, Z.; Fu, R.; Xu, Y.; Bao, X.; Hu, H.; Au-Yeung, S. C. Towards guest-zeolite interactions: an NMR spectroscopic approach. *Chem.—Eur. J.* **2002**, *8* (19), 4557−61.

(143) Hu, Y. L.; Li, M. R.; Hou, G. J.; Xu, S. T.; Gong, K.; Liu, X. C.; Han, X. W.; Pan, X. L.; Bao, X. H. The role of water in methane adsorption and diffusion within nanoporous silica investigated by hyperpolarized 129Xe and 1H PFG NMR spectroscopy. *Nano Res.* **2018**, *11* (1), 360−369.

(144) Xu, S.; Li, X.; Sun, C.; Zheng, A.; Zhang, W.; Han, X.; Liu, X.; Bao, X. Mapping the dynamics of methanol and xenon co-adsorption in SWNTs by in situ continuous-flow hyperpolarized 129Xe NMR. *Phys. Chem. Chem. Phys.* **2019**, *21* (6), 3287−3293.